Assessment of computational tools for MRI RF dosimetry by comparison with measurements on a laboratory phantom

Assessment of computational tools for MRI RF dosimetry by comparison with measurements on a laboratory phantom

O Bottauscio[1$], A M Cassarà[2], J W Hand[3], D Giordano[1], L Zilberti[1], M Borsero[1], M Chiampi[4], G Weidemann[2]

[1] Istituto Nazionale di Ricerca Metrologica (INRIM), Division of Metrology for the Quality of Life, I10135 Torino, Italy

[2] Physikalisch-Technische Bundesanstalt (PTB), D-10587 Berlin, Germany

[3] Division of Imaging Sciences and Biomedical Engineering, King's College London, London SE1 7EH, United Kingdom

[4] Politecnico di Torino, Dipartimento Energia, I-10129 Torino, Italy

E-mail: o.bottauscio@inrim.it

Abstract

This paper presents an extended comparison between numerical simulations using different computational tools employed nowadays in electromagnetic dosimetry and measurements of radiofrequency (RF) electromagnetic field distributions in phantoms with tissue-simulating liquids at 64 MHz, 128 MHz and 300 MHz, adopting a customized experimental setup. The aim is to quantify the overall reliability and accuracy of RF dosimetry approaches at frequencies in use in Magnetic Resonance Imaging transmit coils.

Measurements are compared against four common techniques used for electromagnetic simulations, i.e. the Finite Difference Time Domain (FDTD), the Finite Integration Technique (FIT), the Boundary Element and Finite Element Method (BEM and FEM) approaches. It is shown that FDTD and FIT produce similar results, which generally are also in good agreement with those of FEM-BEM. On the contrary, BEM seems to perform less well than the other methods and shows numerical convergence problems in presence of metallic objects.

Maximum uncertainties of about 30% (coverage factor k = 2) can be attributed to measurements regarding electric and magnetic field amplitudes. Discrepancies between simulations and experiments are found to be in the range from 10% to 30%. These values confirm other previously published results of experimental validations performed on a limited set of data and define the accuracy of our measurement setup.

1. Introduction

Magnetic Resonance Imaging (MRI) and Computer Tomography (CT) are today's main medical imaging modalities and have contributed to significant developments in medical visualization (Botha *et al* 2012). The great advantages of MRI over CT are that it does not require ionizing radiation and provides three-dimensional images of tissue functionality, as well as anatomy, with millimetric or sub-millimetric spatial resolution. Moreover, its adjustable contrast capabilities, particularly with respect to soft tissue, cannot be provided by any other imaging modality. For all these reasons, MRI is an indispensable tool in diagnosis and therapy control of neurologic, oncologic, cardiovascular, or musculoskeletal diseases.

[$] Author to whom any correspondence should be addressed.

General guidelines for human exposure to static magnetic and time-varying (up to 300 GHz) electric and magnetic fields are provided by the International Commission on Non-Ionizing Radiation Protection (ICNIRP) (ICNIRP Guidelines, 1998, 2009, 2010 and 2014). Basic restrictions are given in terms of dosimetric quantities (induced electric field (E-field) and specific absorption rate (SAR)); related reference levels are expressed in terms of externally measurable field quantities. MRI specific safety issues for patients are the subject of ICNIRP guidelines published in 2009 (ICNIRP Statement Amendment, 2009). Safety of MRI patients and related workers is also covered by the international standard EN/IEC 60601-2-33 (EN/IEC 60601-2-33, 2010).

Public concerns regarding MRI safety were highlighted by discussions around occupational safety aspects of exposure to electromagnetic (EM) fields. In the process of developing the final Directive (Directive 2013/35/EU, 2013), it became evident how regulatory decision making in this area was partly based on non-metrological and highly disputed input data.

With regard to radiofrequency (RF) heating, recent progress in the scientific literature has suggested that control of the whole body averaged SAR alone is not sufficient to estimate local energy deposition in human tissues, thus opening the road to the estimation of local SAR and the consequent adoption of local limits for this quantity (Wang *et al* 2007). The inconsistency between existing limits for global and local SAR becomes particularly evident as the B_0 field is increased (> 1.5 T), and consequently as the frequency of the B_1 field is increased (> 64 MHz) (Nelson *et al* 2013).

Furthermore, there is increasing interest in extending MRI applications to patients with medical implants, who are today substantially excluded from evaluation. This need requires the assessment of the specific risks of possible excessive heating due to EM effects induced by RF and gradient coils, when considering bulk metallic prostheses (such as hip prostheses). ASTM F2182 (ASTM F2182 Standard, 2011) and ISO/TS 10974 (ISO/TS 10974, 2012) are currently the Standards that address the assessment of the safety of magnetic resonance imaging for patients with an implanted medical device. They also provide basic test methodologies for testing devices against RF heating. On this topic, the interlaboratory comparison study published by Kainz et al. (Kainz *et* al., 2009) has shown a wide variability of results in terms of temperature elevation, even if measurements are performed according to guidelines; starting from this work, Neufeld et al. (Neufeld *et* al., 2009) showed that the uncertainty can be considerably reduced if appropriate instrumentation and procedures are adopted.

Although the control of excessive heating and temperature increase is the final goal of RF dosimetry in MRI (Oh *et* al., 2014), prediction of local SAR is still a relevant physical quantity to be monitored and compared with human exposure limits. Moreover, the need for accurate prediction of the local energy deposition is often pointed out as fundamental to improve temperature increase estimation (Neufeld *et* al., 2009, Wolf *et* al., 2013).

Since local SAR estimation by invasive measurements within the human body is not feasible, data describing local energy deposition can be reconstructed from complex mapping of B_1^+ field (Zhang *et al* 2013) through suitable algorithms based on simplifying assumptions, or acquired from experiments performed in-vivo on animals or on phantoms (Bassen *et al* 2009, Oh *et al* 2010, Voigt *et al* 2012, Gorny *et al* 2013). Alternatively, computational codes based on the solution of Maxwell's equations are often used to predict local distributions of electromagnetic fields and SAR. These numerical approaches take advantage of the rapid development over the last few years of new numerical algorithms combined with relatively low cost powerful computational resources (e.g. Graphic Processing Units), as well as the availability of more and more sophisticated numerical anatomical human models (Collins *et al* 2011, Powell *et al* 2012, Voigt *et al* 2012, van Lier *et al* 2012, Wilkoff *et al* 2013, Cabot *et al* 2013, Bottauscio *et al* 2014).

A large variety of commercial or open-source program packages exists, being capable of producing quantitatively correct results in the electromagnetic field simulations. The most popular and efficient numerical techniques are the finite difference time domain (FDTD) and its extensions (Dimbylow *et al* 1991, De Raedt *et al* 2003, Clemens *et al* 2012), largely adopted in electromagnetic dosimetry (see for example Samaras *et al* 2000 and Bernardi *et al* 2002), and the finite integration technique (FIT) (Weiland, 1977). These two methods are implemented within widely used commercial software, such as SEMCAD X MED (SPEAG AG, Zurich) and CST Microwave Studio® (Computer Simulation Technology, Darmstadt)). Other adopted methodologies used in computational dosimetry and developed at the level of research groups are the finite element method (FEM) (Ilvonen *et al* 2009, Laakso *et al* 2012, Ruoff *et al* 2012), the boundary element method (BEM) (Bottauscio *et al* 2012), the method of moments (MoM) (Cimala *et al* 2013), lumped-parameter approaches (Nagai *et al* 2009) and hybrid techniques, which combine different numerical methods (e.g. FEM-BEM in (Bottauscio *et al* 2014)). While FDTD and FIT are intrinsically developed in the time-domain, frequency-domain solvers can be implemented by using the other numerical methods.

The use of computational tools in MRI safety calls for methods and procedures capable of testing the reliability of the dosimetric simulations, in order to avoid result inaccuracies as documented in literature (see for example Collins *et al* 2003 and Zelinski *et al* 2008). Several validations of dosimetric simulations related to non-MRI applications have been published (see for example Gajsek *et al* 2002, Pisa *et al* 2005, Bamba *et al* 2013), resulting in deviations with respect to experiments from a few percent to almost one hundred percent, depending on the field exposure scenario. With specific reference to MRI dosimetry, some papers address the problem of validation of numerical prediction, using phantoms, comparison with alternative solutions or in-vivo measurements. Most of them rely on FDTD modeling, often limiting the comparisons to a few measurement points and focusing on the temperature increase within the phantom (see for example Nguyen *et al* 2004) or in close proximity of conducting wires simulating DBS devices (Mohsin *et al* 2008, Elwassif *et al* 2012, Cabot *et al* 2013). Comparisons with measured local SAR at the tip of a metal implant within a phantom were also published (Mattei *et al* 2010). In the work of Kangarlu *et al* 2007, the spatial distribution of the electric field within a saline water phantom radiated by a 8 T RF head coil is qualitatively compared with experiments. Amjad *et al* 2005 compare temperature increase in the ASTM phantom placed inside a whole body bird-cage coil (64 MHz). Discrepancies between simulations and experiments vary in a range between 15% and 100% depending on the quantity under analysis and the procedure adopted for the comparison.

Other papers compare SAR distributions more at a qualitative level (Oh *et al*. 2010), with the aim of evaluating the capability of predicting the spatial distribution of “hot spots”. Validations with in-vitro body phantoms are also performed in terms of measured power and FDTD simulations adopting SEMCAD software (Wilkoff *et al* 2013). In other cases, comparisons with experiments on laboratory phantoms are performed with the aim of understanding the effect of numerical approximations on the simulation quality (Voigt *et al* 2012).

Validation with experiments are also used to evaluate the capability of the numerical tools in predicting the field generated by MR sources. As an example, hybrid methods based on MoM-FDTD and MoM-FEM are tested considering RF coils (Li *et al* 2009).

Comparison between the numerical results of two different commercial electromagnetic software packages (HFSS (ANSYS, Canonsburg, PA) and CST Microwave Studio®), applied to the exposure of a human head to the RF field of a 7 T multi-channel coil, are reported by Kozlov *et al* 2010, showing agreement within 15% for the induced electric field.

Capstick *et al* 2008 use FDTD (SEMCAD X) and FIT (CST Microwave Studio) to simulate RF fields associated with a range of MR scanners (1.5 T, 3 T, and 7 T conventional cylindrical bore scanners and a 1 T open scanner) and compare results with measurements of E- and H- fields.

The purpose of this work is to provide a systematic comparison between experiments and simulations using different methodologies and computational codes and thereby contribute to the analysis of accuracy in computational estimation of local SAR. Attention is here not focused on the effect of computational parameters (e.g. geometrical discretization, convergence, etc.), which is the scope of several published papers for a variety of different physical problems, not limited to MR dosimetry (see for example *Murbach et al* 2014). The comparison with experiments was here intended to quantify discrepancies due to the systematic errors, which are inevitably introduced in the virtual model. For this reason, in our simulations, numerical solutions have been always "stabilized", trying to preliminarily find the most appropriate spatial/time discretization for each considered case under study.

To the purpose of the comparison with experiment, electromagnetic field measurements have been made traceable to SI units, introducing a detailed uncertainty budget of measurement results to assess the reliability of experiments. The analysis is focused on exposure conditions that mimic the RF fields generated by generic surface MRI coils of 1.5 T (64 MHz), 3 T (128 MHz) and 7 T (300 MHz) scanners.

2. Materials and methods

2.1 Laboratory setup

A laboratory setup has been developed to enable electromagnetic field measurements to be made in a phantom mimicking the properties of human tissues at MRI radio-frequencies. The phantom consists of a cylindrical box (diameter 240 mm, height 240 mm) filled with a tissue-simulating liquid (TSL). The material (PolyMethylMethAcrylate (Plexiglass)) and the thickness of the vessel walls (3 mm) were chosen to limit the distortion of the electromagnetic field generated by the source; preliminarily simulations verified that their effect was negligible.

The phantom is located within a structure which supports the field source and the gantry for positioning the field probes within the liquid (Figure 1). The support is made of PolyOxyMethylene (Delrin), without metallic parts to reduce field distortion due to induced effects.

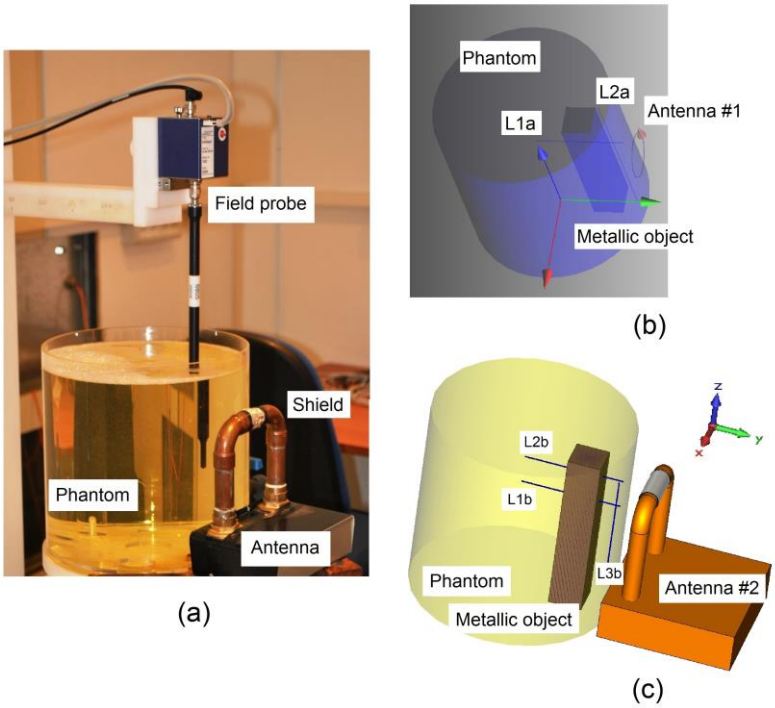

FIG 1. View of the experimental setup with the antenna #2 (a); schemes of the phantom with the antenna #1 (b) and the antenna #2 (c). The investigation lines L1a and L2a (for antenna #1) and L1b, L2b and L3b (for antenna #2), defined in Section 3.2, are shown in the scheme.

A reference frame is located in the centre of the bottom side of the phantom, with the *z*-axis along the cylinder axis and the *y*-axis parallel to the antenna axis. Large metallic bodies can be located within the phantom to simulate the presence of passive implants and to monitor the distortions of the field distribution around the object. In the experiments presented below, a non-magnetic metallic parallelepiped (1.35 MS/m electrical conductivity) with a (40 × 40) mm^2 cross section and a height of 200 mm is placed parallel to the z-axis at 105 mm from the origin.

The TSL is made of 70.73% water, 28.33% polysorbate20 and 0.93% NaCl (by weight) and mimics the average dielectric properties of human body tissue at a frequency of 150 MHz (Loader *et al* 2010). Human tissue data originate from the works of Gabriel et al. (Gabriel *et al* 1996a, 1996b, 1996c), being widely available thanks to some online databases (Andreuccetti *et al* 2000 and Hasgall *et al* 2013). Electrical conductivity and permittivity of the TSL have been characterized in the frequency range from 50 MHz to 300 MHz and in the temperature range between 10 °C and 27 °C, using an open-ended coaxial probe (for a description of the method see Athey *et al* 1982 and Stuchly *et al* 1982) and a vector network analyzer (HP 4396B with directional coupler HP43961S) for the measurement of the reflection coefficient. The tip capacitance was determined from reference measurements of distilled water. Figure 2 shows the dependence of permittivity and electrical conductivity on frequency and temperature respectively.

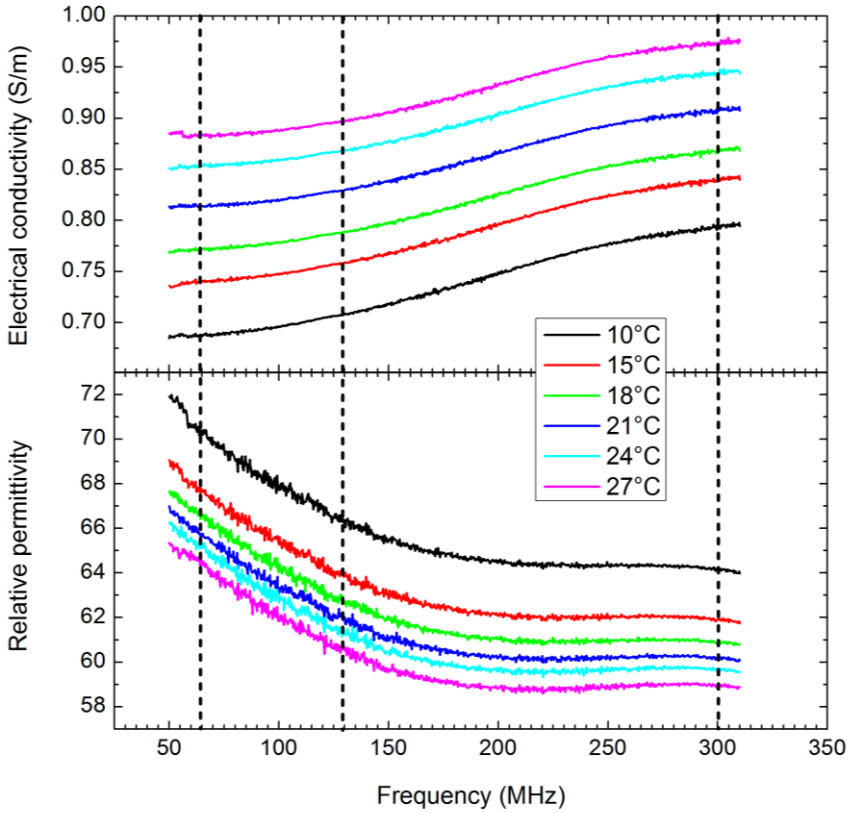

FIG 2. Dependence of TSL electrical conductivity and relative permittivity on frequency and temperature

Antennas similar to a surface MRI RF coil having two different shapes and dimensions are used to radiate the phantom.

The use of this type of antennas reduces the unavoidable errors related to the simulation of more complex systems (e.g. birdcage antenna) and increases the field spatial gradients, making the numerical analysis more severe.

The first antenna (#1) is a small loop, consisting of a single turn of 60 mm diameter, inside a balanced E-field shield (see Fig 1b). This loop can generate a magnetic field in air equal to 1 A/m at a distance of 20 mm along the loop axis, with an input current of about 0.5 A. This value is lower than the typical magnetic field value generated by an RF coil of the MRI devices; nevertheless, the estimated electric field induced by such magnetic field within the phantom is a few tens of volts per meter, which provides an acceptable signal-to-noise ratio. The internal lead of the antenna is placed at 133 mm from the *z*-axis, along the *y*-axis.

The second antenna (#2) has a square shape with a greater size (120 × 105 mm^2), to increase the phantom's radiated area (see Fig 1c). A shield around the lead wire, made of two ground-connected sections and a floating one, is introduced to reduce the electric field concentration near the supply terminals. This antenna can generate a magnetic field equal to 2 A/m at a distance of 43 mm along the loop axis, with an input current of about 0.4 A. The internal lead of the antenna is placed at a distance of 153 mm from the *z*-axis along the *y*-axis. Details about the antenna supply system, the characterization of the antenna equivalent circuit and the measuring setup can be found in Giordano *et al* 2013.

E and **H** fields are measured within the liquid by isotropic probes (H3DV8 H-field probe and ER3DV6 E-field probe, (SPEAG AG, Zurich)). These isotropic probes give the true rms value of the applied field along the three orthogonal axes. The main characteristics of the probes are summarized in Table I. The field generation and detection system is automatically managed by a Python program.

A budget of the measurement uncertainty has been estimated for the magnetic and electric field components, taking into account the most relevant contributions to the measurement error: *i*) possible temperature oscillations during the measurement stage, *ii*) possible positioning errors of the field probes and *iii*) probe inaccuracy. The details of the measurement model are reported in Appendix, where the procedure recommended in JCGM (JCGM, 2008) has been adopted. The resulting uncertainty (assuming a coverage factor $k = 2$) has been associated to the measurement values in the diagrams reported in Section 3.

TABLE I. Characteristics of the electric and magnetic field probes

	Electric field (ER3DV6)	Magnetic Field (H3DV8)
Frequency	40 MHz to 6 GHz	10 MHz to 600 MHz (absolute accuracy (2σ) ± 6.0%)
Dynamic range	2 V/m to 1000 V/m	0.02 A/m to 8 A/m at 64 MHz 0.008 A/m to 4 A/m at 128 MHz 0.003 A/m to 1.7 A/m at 300 MHz
Overall length:	337 mm (tip: 40 mm)	337 mm (tip: 40 mm)
Distance from probe tip to dipole centre	2.5 mm	3 mm
External tip diameter	8 mm	6 mm

2.2 EM field computations

Four numerical simulations tools having different characteristics and therefore different merits and drawbacks have been considered, namely Finite Difference Time Domain (FDTD), Finite Integration Technique (FIT), Boundary Element Method (BEM), and coupled Finite Element – Boundary Element (FEM-BEM) Technique.

FDTD is the most commonly used technique for electromagnetic dosimetry (Samaras *et al* 2000, Liu *et al* 2008), based on the Yee algorithm (Yee 1966), being a versatile and intuitive modeling technique suitable for voxel-based models. It works in the time-domain, and through the use of a broadband pulse, the response over a wide range of frequencies can be obtained with a single simulation. Its main drawbacks are: the whole space separating the source and the object must be discretized; artificial boundary conditions are needed to handle open-boundary domains; steady-state solutions are obtained simulating the whole transient time response of the system and this can result in very long simulation times for strong resonators. This method has been implemented in several commercial software packages. The results reported in this paper have been obtained using the software SEMCAD-X vs.14.8.5 (SPEAG AG, Zurich).

FIT (Weiland, 1977) is an efficient numerical technique, largely employed in microwave, radio-frequency and EMC simulations. Maxwell's equations are handled by adopting integral unknowns on a set of staggered grids. Following this formulation, the use of a consistent dual orthogonal grid in conjunction with an explicit time integration scheme leads to computational and memory-efficient algorithms. FIT shows similar drawbacks as FDTD. The results reported in this paper have been obtained using the software CST Microwave Studio® version 2014 (Computer Simulation Technology, Darmstadt).

BEM is a technique that solves boundary value problems in their integral form by adopting the Green function as a spatial reconstructor. It requires calculating only boundary domain field values (Brebbia *et al* 1980). It can be formulated in the frequency domain and it does not need bounded domains, thus it is tailored for far field evaluations. A drawback is that it gives rise to fully populated matrices, which often results in significantly less efficient codes than volume-discretization methods; moreover, BEM is intrinsically suited for homogenous or weakly non-homogeneous domains, so that it cannot be directly applied to voxel-based models. Anyway, it has been applied in literature to MRI dosimetry analysis for voxel-based models (see for example Hamada *et al* 2011) or phantom models (Bottauscio *et al* 2011), thus we believe useful to include this method in the error analysis. An original code has been developed to produce the numerical results reported in this paper. For details about this method see (Bottauscio *et al* 2012).

To overcome the limits of BEM in processing highly non-homogenous models, while keeping its advantages in handling open-boundary domains, coupled field formulations have been proposed in literature (D'Angelo 1989, Nguyen *et al* 2002). Since FEM is well suited for non-homogeneous domains with complex shape, it is used here to solve the field within the phantom (voxel-based model), while BEM is applied to the external open-boundary domain. This formulation can be developed in the frequency domain. A FEM-BEM hybrid code has been specifically developed and used to produce the numerical results reported in this paper. For details about this method see (Bottauscio *et al* 2015), while additional information about GPU hardware acceleration specifically adopted for this kind of implementation can be found in Bottauscio *et al* 2014.

FEM has not been considered in the present analysis, being inappropriate for open boundary domain problems. It always requires the use of proper techniques for handling domain boundaries, such as absorption boundary conditions (see for example Ruoff *et al* 2012), leading to numerical implementations similar to hybrid FEM-BEM approaches.

Both for BEM and FEM-BEM models the field sources are assumed to be ideal, which means the current is impressed within the antenna lead and it is not altered by the presence of the phantom.

3. Results

The numerical tools previously introduced have been applied to the evaluation of the electromagnetic field within and around the phantom radiated by the antennas used in the experiments. The experimental conditions have been reproduced, imposing a sinusoidal current in the antennas at frequencies of 64 MHz, 128 MHz and 300 MHz. The electrical conductivity and relative permittivity of the TSL have been fixed respectively at 0.86 S/m and 65 for 64 MHz, 0.87 S/m and 61.5 for 128 MHz and 0.94 S/m and 59.5 for 300 MHz, assuming the values measured at 24 °C, i.e. the temperature recorded during the experiments.

In the simulations performed by FDTD, FIT and FEM–BEM, the phantom and the metallic object (when present) are discretized into $2\times2\times2$ mm^3 voxels. The minimum grid cell dimension in FDTD and FIT was 0.5 mm. BEM simulations have been performed with quadrangular surface elements of 2×2 mm^2. In time-domain FDTD and FIT simulations, time step ranges from 10^{-13} s to 10^{-12} s. The tolerance of residual variations to stop iterations was set at -40dB.

For FIT simulations a bounding box spaced at $\lambda/8$ from structures (where λ is the wavelength at the considered frequency) was defined and used to apply open boundary conditions. In the case of FDTD simulations absorbing

boundaries using uniaxial perfectly matched layers bounded the computational domain spaced at λ/4 from structures. No artificial boundary conditions are needed in BEM and FEM-BEM.

3.1 Results with antenna #1

This set of results was obtained with the circular loop antenna (#1), at 64 MHz, 128 MHz and 300 MHz. The position of the centre of the loop antenna, with respect to the phantom reference frame, is: $x_c = 0$, $y_c = 133$ mm, $z_c = 120$ mm. The phantom has been radiated without the presence of the metallic object and the results are compared along a radial line (line L1a: from point {0,0,150} mm to point {0,120,150} mm) and a vertical line (line L2a: from point {0,110,0} mm to point {0, 110, 240} mm). The computed and experimental results have been rescaled to the magnetic field amplitude H_{ref} at the end of line L1a (point {0,120,150} mm), which is provided by each considered method (or experiment). The comparison has been limited to the main field components, namely the *y*- and *z*-components for the **H** field and the *x*-component for the **E** field. Figures 3 to 5 show the measured and computed values, obtained at 64 MHz, 128 MHz and 300 MHz respectively.

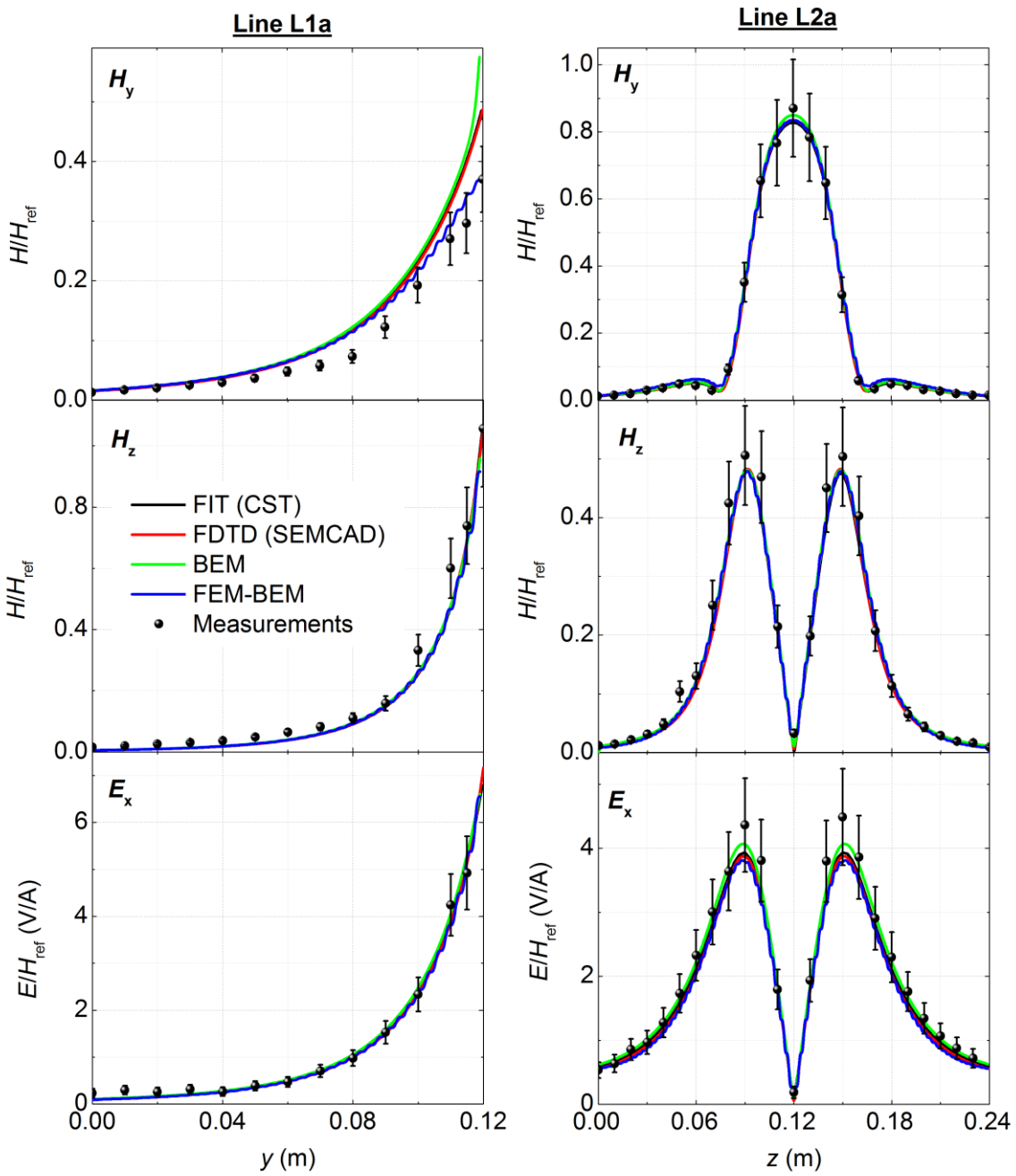

FIG 3. Comparison among measured and computed normalized fields with the phantom radiated by the antenna #1 at 64 MHz. On the left H_y/H_{ref}, H_z/H_{ref} and E_x/H_{ref} along line L1a, on the right H_y/H_{ref}, H_z/H_{ref} and E_x/H_{ref} along line L2a. A coverage factor $k = 2$ has been associated to measurement uncertainties.

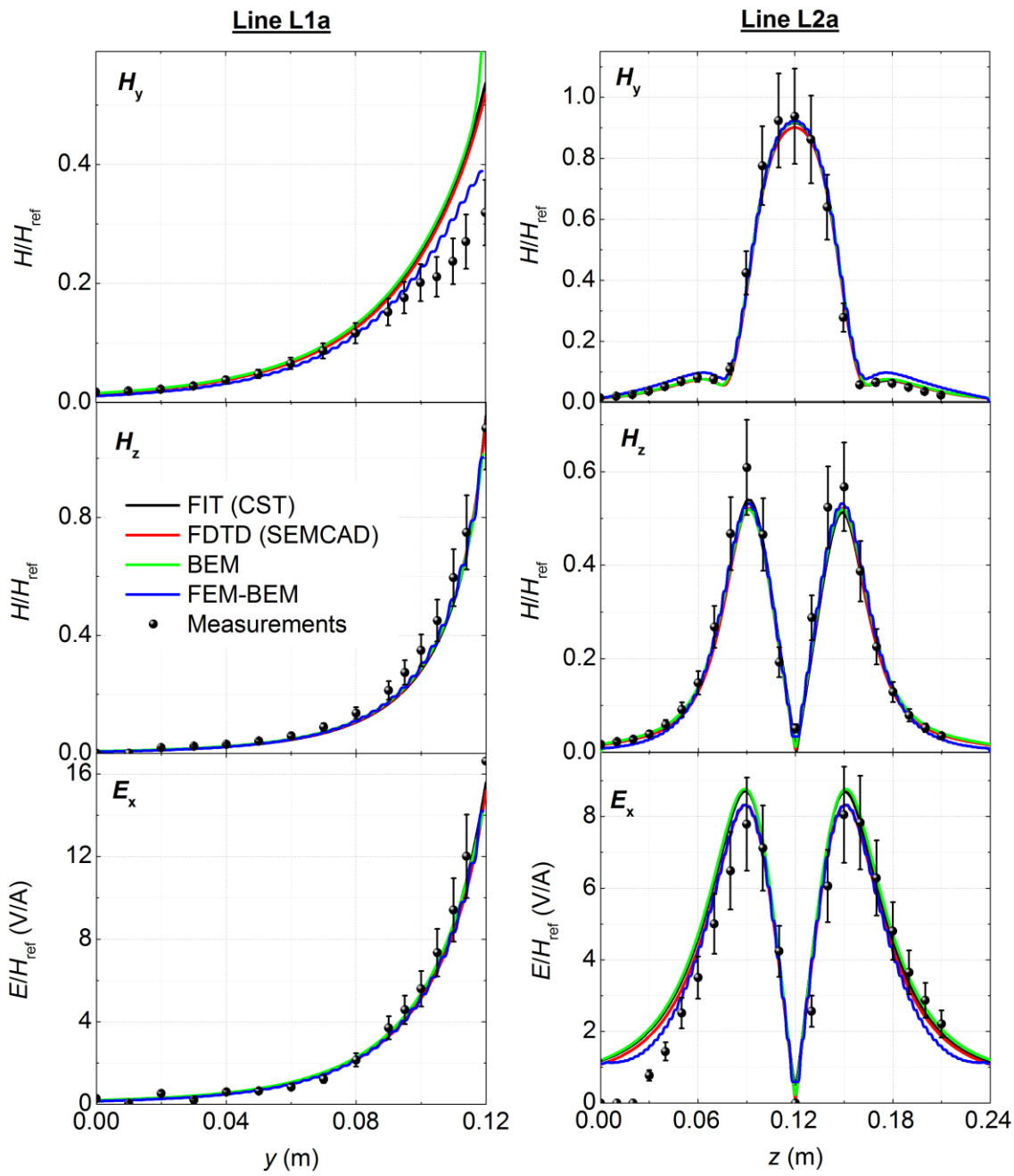

FIG 4. Comparison among measured and computed normalized fields with the phantom radiated by the antenna #1 at 128 MHz. On the left H_y/H_{ref}, H_z/H_{ref} and E_x/H_{ref} along line L1a, on the right H_y/H_{ref}, H_z/H_{ref} and E_x/H_{ref} along line L2a. A coverage factor $k = 2$ has been associated to measurement uncertainties.

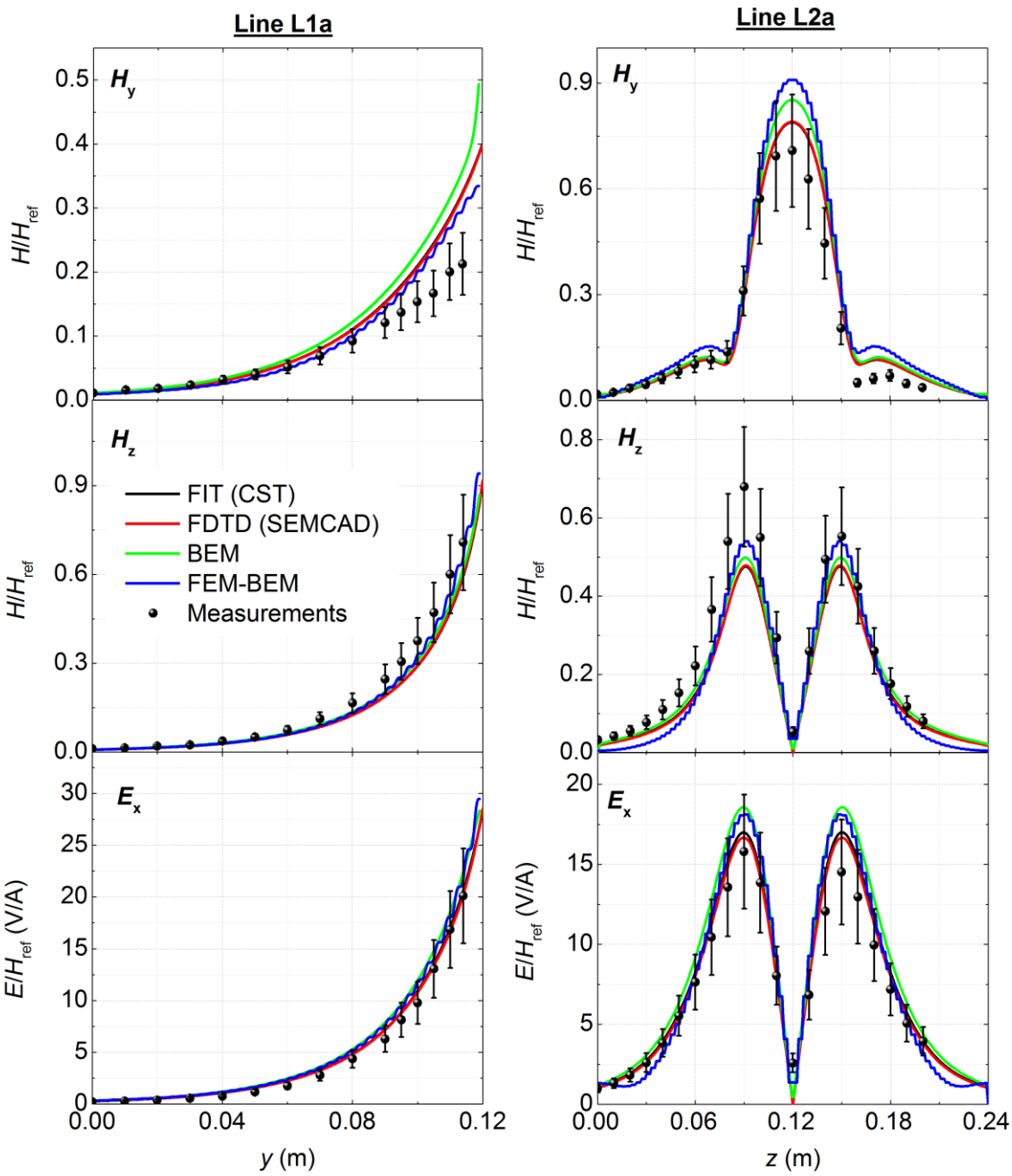

FIG 5. Comparison among measured and computed normalized fields with the phantom radiated by the antenna #1 at 300 MHz. On the left H_y/H_{ref}, H_z/H_{ref} and E_x/H_{ref} along line L1a, on the right H_y/H_{ref}, H_z/H_{ref} and E_x/H_{ref} along line L2a. A coverage factor k = 2 has been associated to measurement uncertainties.

3.2 Results with antenna #2 without metallic object

This set of results was obtained with the square antenna (#2) at 64 MHz and 128 MHz; the larger dimensions of this antenna make it not suitable for a frequency of 300 MHz. The position of the centre of the antenna is: x_c = 0, y_c = 153 mm, z_c = 120 mm. The phantom has been radiated without the metallic object and the results are compared along two radial lines (line L1b: from point {0, -5, 148} mm to point {0, 115, 148} mm and line L2b: from point {0, -5, 183 mm} mm to point {0, 115, 183} mm) and a vertical line (line L3b: from point {0, 113, 10} mm to point {0, 113, 200} mm).

The computed and experimental results have been rescaled to the corresponding magnetic field amplitude H_{ref} at the end of line L1b (point {0, 115, 148} mm).The comparison has been limited to the main field components, namely the *y*- and *z*-components for the **H** field and the *x*-component for the **E** field. Figures 6 and 7 show the measured and computed values, obtained at 64 MHz and 128 MHz respectively.

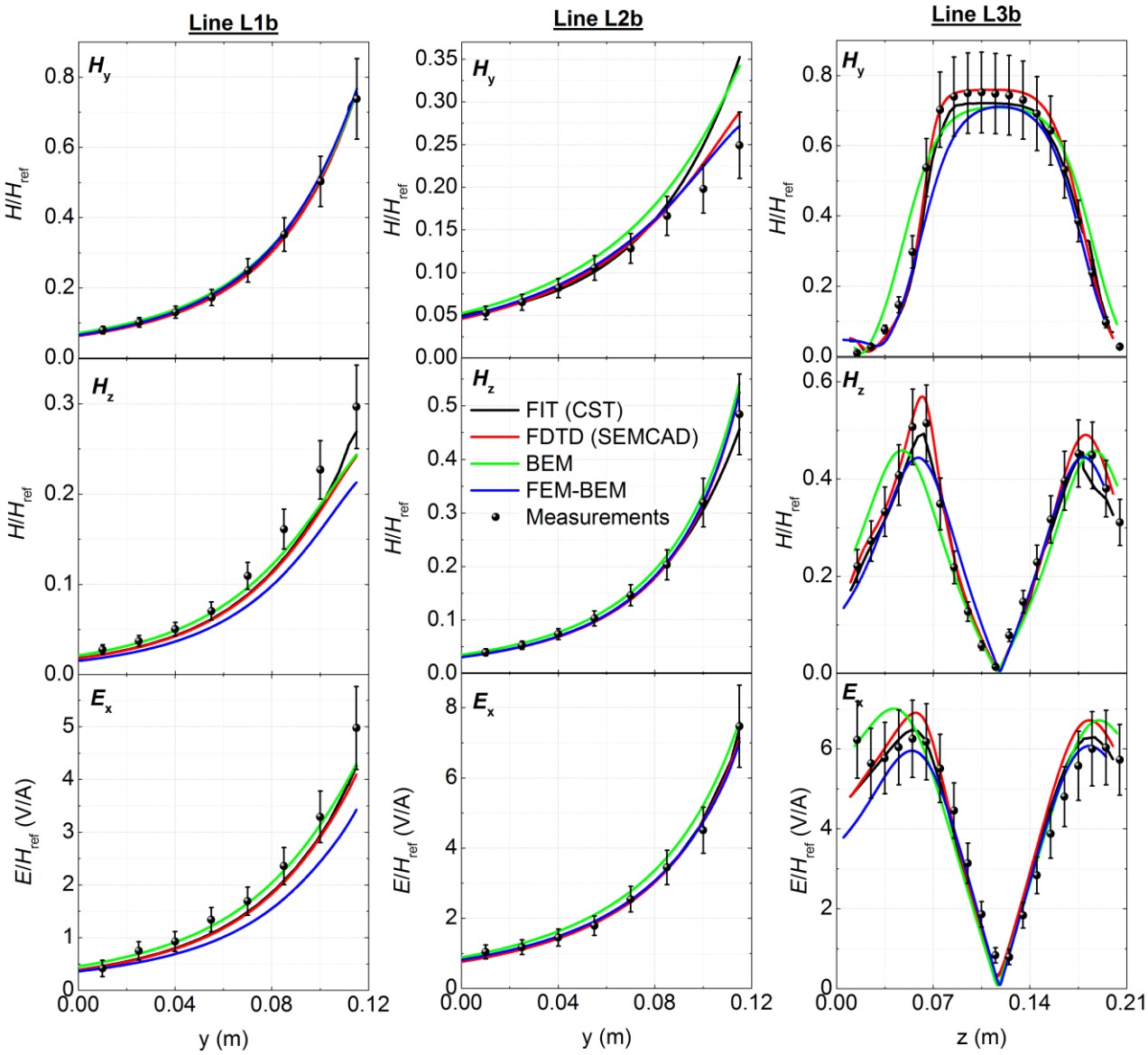

FIG 6. Comparison among measured and computed results with the phantom radiated by the antenna #2 without the metallic object at 64 MHz. From left to right: a) H_y/H_{ref}, H_z/H_{ref} and E_x/H_{ref} along line L1b, b) H_y/H_{ref}, H_z/H_{ref} and E_x/H_{ref} along line L2b, c) H_y/H_{ref}, H_z/H_{ref} and E_x/H_{ref} along line L3b. A coverage factor k = 2 has been associated to measurement uncertainties.

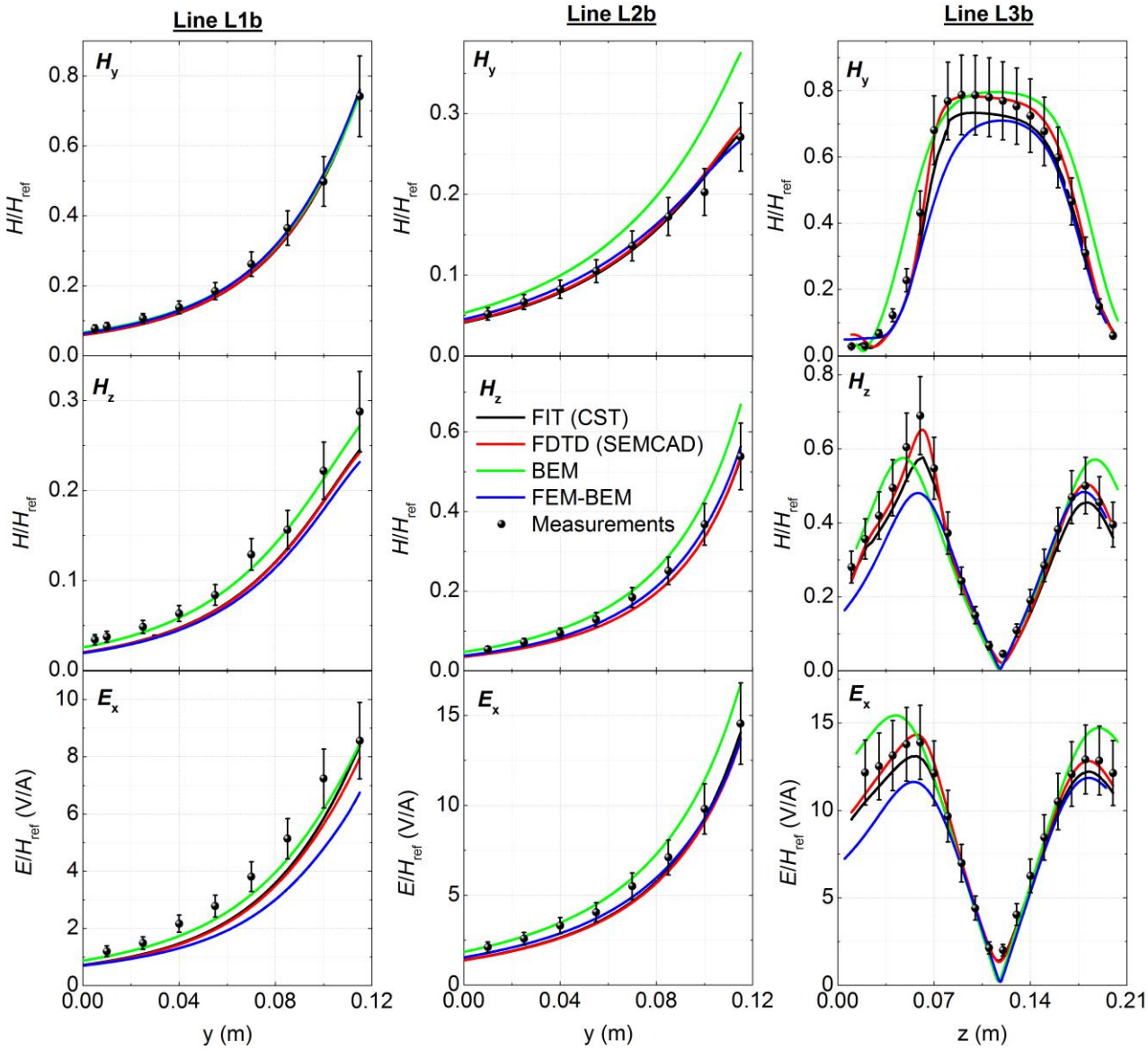

FIG 7. Comparison among measured and computed results with the phantom radiated by the antenna #2 without the metallic object at 128 MHz. From left to right: a) H_y/H_{ref}, H_z/H_{ref} and E_x/H_{ref} along line L1b, b) H_y/H_{ref}, H_z/H_{ref} and E_x/H_{ref} along line L2b, c) H_y/H_{ref}, H_z/H_{ref} and E_x/H_{ref} along line L3b. A coverage factor k = 2 has been associated to measurement uncertainties.

3.3 Results with antenna #2 in the presence of the metallic object

This set of results was obtained with the same square antenna (#2) as reported in Section 3.2, but in presence of the metallic object. Simulations and experiments have been performed at 64 MHz and 128 MHz. The results are compared along a radial line (line L2b: from point {0, -5, 183} mm to point {0, 115, 183} mm) and a vertical line (line L3b: from point {0, 113, 10} mm to point {0, 113, 200} mm). Also for this set of results, the field values have been rescaled to the magnetic field amplitude H_{ref} at the end of line L1b (point {0, 115, 148} mm) and the comparison has been limited to the most relevant field components, namely the *y*- and *z*-components for the **H** field and the *x*-component for the **E** field.

In the presence of the metallic object, BEM failed to provide reliable results due to difficulties in the convergence of the GMRES iterative algorithm for the matrix solution, arising from bad conditioning of the matrix, which includes BEM elements on the metal surface with high discontinuities in electrical properties. For this reason, only results obtained with FIT, FDTD and FEM-BEM at 64 MHz and 128 MHz are reported in Figures 8 and 9, together with measurements. Results along investigation line L1b are similar to those obtained along line L2b and are not reported here.

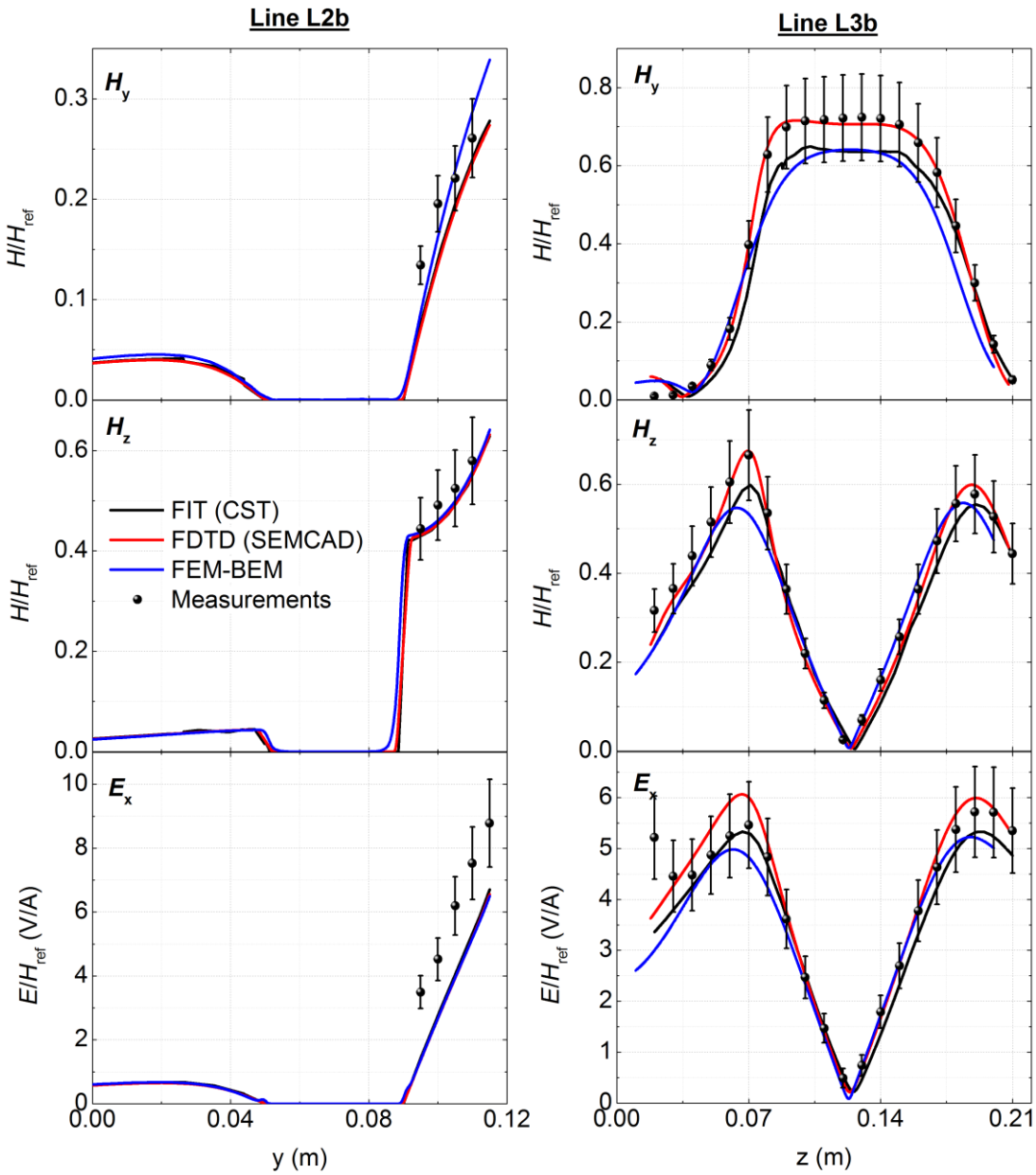

FIG 8. Comparison among measured and computed results with the phantom radiated by the antenna #2 at 64 MHz in presence of the metallic object. On the left H_y/H_{ref}, H_z/H_{ref} and E_x/H_{ref} along line L2b, on the right H_y/H_{ref}, H_z/H_{ref} and E_x/H_{ref} along line L3b. A coverage factor $k = 2$ has been associated to measurement uncertainties.

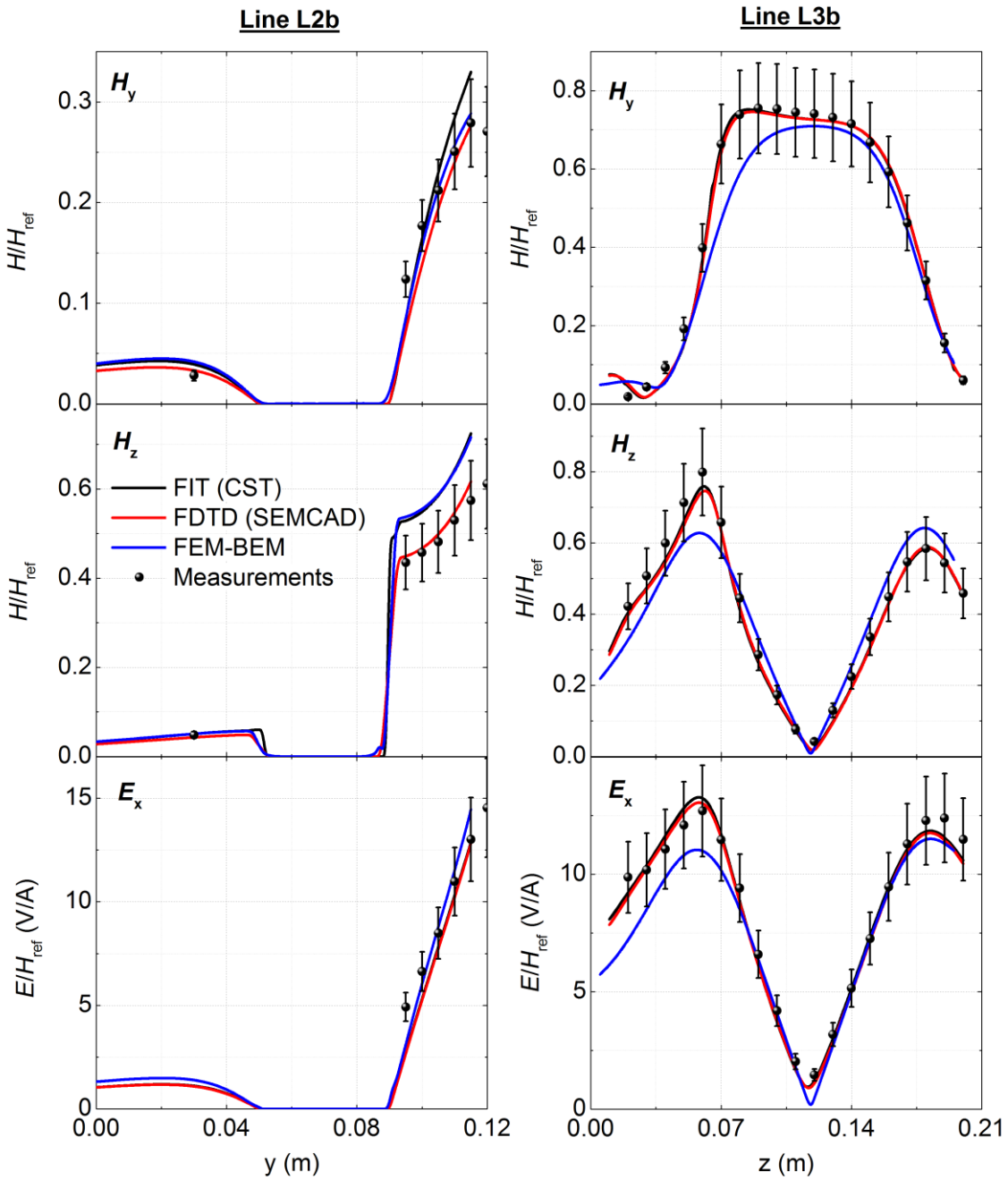

FIG 9. Comparison among measured and computed results with the phantom radiated by the antenna #2 at 128 MHz in presence of the metallic object. On the left H_y/H_{ref}, H_z/H_{ref} and E_x/H_{ref} along line L2b, on the right H_y/H_{ref}, H_z/H_{ref} and E_x/H_{ref} along line L3b. A coverage factor $k = 2$ has been associated to measurement uncertainties.

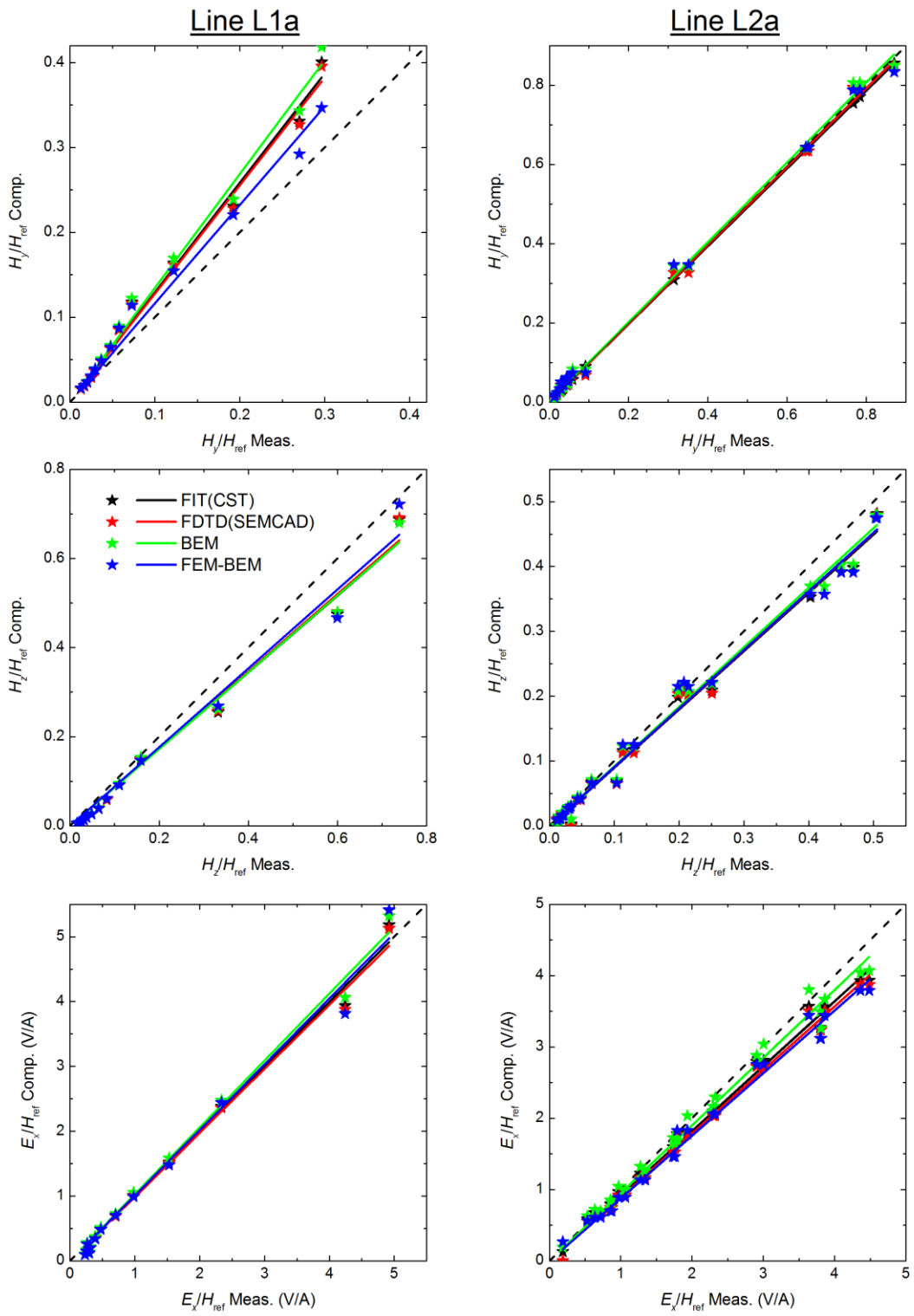

FIG 10. Computational results (c) plotted versus the corresponding measurement points (m) and fitted by linear interpolation ($c = a \cdot m$), corresponding to data reported in Fig. 3 (antenna #1 at 64 MHz).

TABLE. II. Coefficient of linear interpolation a with its expanded uncertainty $U(a)$ for the results of computations with FIT(CST) reported in Figs. 3 to 9. Values of parameter a greater than 1.3 or lower than 0.7 are highlighted.

Frequency (MHz)	Metallic object	Investigation line	Figure with raw data	$a \pm U(a)$		
				Related to quantity H_y/H_{ref}	Related to quantity H_z/H_{ref}	Related to quantity E_x/H_{ref}
64	NO	L1a	3	1.29 ± 0.11	0.86 ± 0.09	1.00 ± 0.10
		L2a		0.98 ± 0.07	0.90 ± 0.05	0.91 ± 0.04
128	NO	L1a	4	**1.38 ± 0.08**	0.86 ± 0.07	0.92 ± 0.07
		L2a		0.97 ± 0.07	0.90 ± 0.05	1.09 ± 0.06
300	NO	L1a	5	**1.39 ± 0.12**	0.80 ± 0.08	1.04 ± 0.11
		L2a		1.11 ± 0.10	0.75 ± 0.06	1.11 ± 0.08
64	NO	L1b	6	1.01 ± 0.09	0.86 ± 0.07	0.87 ± 0.08
		L2b		1.22 ± 0.08	0.95 ± 0.09	1.01 ± 0.09
		L3b		0.96 ± 0.04	0.94 ± 0.04	1.00 ± 0.04
128	NO	L1b	7	0.99 ± 0.09	0.84 ± 0.07	0.86 ± 0.06
		L2b		1.01 ± 0.08	0.94 ± 0.08	0.93 ± 0.08
		L3b		0.93 ± 0.04	0.89 ± 0.04	0.93 ± 0.04
64	YES	L2b	8	0.83 ± 0.06	0.95 ± 0.07	**0.65 ± 0.06**
		L3b		0.89 ± 0.04	0.91 ± 0.04	0.91 ± 0.04
128	YES	L2b	9	1.15 ± 0.08	1.25 ± 0.08	0.97 ± 0.07
		L3b		0.99 ± 0.04	0.95 ± 0.04	0.99 ± 0.04

TABLE. III. Coefficient of linear interpolation a with its expanded uncertainty $U(a)$ for the results of computations with FDTD(SEMCAD) reported in Figs. 3 to 9. Values of parameter a greater than 1.3 or lower than 0.7 are highlighted.

Frequency (MHz)	Metallic object	Investigation line	Figure with raw data	$a \pm U(a)$		
				Related to quantity H_y/H_{ref}	Related to quantity H_z/H_{ref}	Related to quantity E_x/H_{ref}
64	NO	L1a	3	1.28 ± 0.11	0.87 ± 0.09	0.99 ± 0.09
		L2a		0.99 ± 0.07	0.90 ± 0.05	0.89 ± 0.04
128	NO	L1a	4	**1.33 ± 0.08**	0.87 ± 0.07	0.88 ± 0.07
		L2a		0.96 ± 0.07	0.89 ± 0.05	1.04 ± 0.05
300	NO	L1a	5	**1.38 ± 0.12**	0.81 ± 0.08	1.03 ± 0.11
		L2a		1.11 ± 0.11	0.75 ± 0.06	1.09 ± 0.07
64	NO	L1b	6	1.01 ± 0.09	0.81 ± 0.07	0.84 ± 0.08
		L2b		1.10 ± 0.08	1.04 ± 0.05	0.98 ± 0.09
		L3b		1.02 ± 0.04	1.05 ± 0.04	1.05 ± 0.04
128	NO	L1b	7	0.99 ± 0.09	0.83 ± 0.07	0.83 ± 0.06
		L2b		1.04 ± 0.07	0.94 ± 0.08	0.91 ± 0.08
		L3b		1.01 ± 0.04	0.96 ± 0.04	0.99 ± 0.04
64	YES	L2b	8	0.80 ± 0.06	0.94 ± 0.07	**0.63 ± 0.05**
		L3b		1.00 ± 0.04	0.98 ± 0.04	1.02 ± 0.04
128	YES	L2b	9	0.97 ± 0.06	1.07 ± 0.06	0.97 ± 0.07
		L3b		0.99 ± 0.04	0.95 ± 0.04	0.97 ± 0.04

TABLE. IV. Coefficient of linear interpolation a with its expanded uncertainty $U(a)$ for the results of computations with BEM reported in Figs. 3 to 9. Values of parameter a greater than 1.3 or lower than 0.7 are highlighted.

Frequency (MHz)	Metallic object	Investigation line	Figure with raw data	$a \pm U(a)$		
				Related to quantity H_y/H_{ref}	Related to quantity H_z/H_{ref}	Related to quantity E_x/H_{ref}
64	NO	L1a	3	**1.34 ± 0.12**	0.86 ± 0.09	1.03 ± 0.10
		L2a		1.01 ± 0.07	0.92 ± 0.05	0.95 ± 0.04
128	NO	L1a	4	**1.40 ± 0.09**	0.87 ± 0.07	0.93 ± 0.08
		L2a		0.97 ± 0.08	0.90 ± 0.05	1.10 ± 0.06
300	NO	L1a	5	**1.54 ± 0.07**	0.84 ± 0.04	1.14 ± 0.06
		L2a		1.20 ± 0.06	0.80 ± 0.03	1.22 ± 0.04
64	NO	L1b	6	1.03 ± 0.09	0.84 ± 0.07	0.91 ± 0.08
		L2b		1.27 ± 0.09	1.09 ± 0.10	1.07 ± 0.10
		L3b		0.98 ± 0.04	0.96 ± 0.04	1.06 ± 0.04
128	NO	L1b	7	1.00 ± 0.09	0.95 ± 0.08	0.90 ± 0.07
		L2b		**1.33 ± 0.10**	1.19 ± 0.10	1.14 ± 0.10
		L3b		1.07 ± 0.05	0.99 ± 0.04	1.08 ± 0.04
64	YES	L2b	8	-	-	-
		L3b		-	-	-
128	YES	L2b	9	-	-	-
		L3b		-	-	-

TABLE. V. Coefficient of linear interpolation a with its expanded uncertainty $U(a)$ for the results of computations with FEM-BEM reported in Figs. 3 to 9. Values of parameter a greater than 1.3 or lower than 0.7 are highlighted.

Frequency (MHz)	Metallic object	Investigation line	Figure with raw data	$a \pm U(a)$		
				Related to quantity H_y/H_{ref}	Related to quantity H_z/H_{ref}	Related to quantity E_x/H_{ref}
64	NO	L1a	3	1.16 ± 0.10	0.88 ± 0.09	1.01 ± 0.09
		L2a		1.00 ± 0.07	0.90 ± 0.05	0.88 ± 0.04
128	NO	L1a	4	1.17 ± 0.07	0.85 ± 0.07	0.86 ± 0.07
		L2a		0.98 ± 0.08	0.91 ± 0.06	1.03 ± 0.05
300	NO	L1a	5	1.29 ± 0.11	0.87 ± 0.09	1.09 ± 0.12
		L2a		1.28 ± 0.12	0.83 ± 0.06	1.16 ± 0.08
64	NO	L1b	6	1.03 ± 0.09	0.71 ± 0.06	0.71 ± 0.06
		L2b		1.09 ± 0.08	1.05 ± 0.10	0.98 ± 0.09
		L3b		0.90 ± 0.04	0.95 ± 0.04	0.94 ± 0.04
128	NO	L1b	7	1.01 ± 0.09	0.79 ± 0.06	0.71 ± 0.05
		L2b		1.02 ± 0.08	1.00 ± 0.09	0.93 ± 0.08
		L3b		0.87 ± 0.04	0.85 ± 0.04	0.86 ± 0.04
64	YES	L2b	8	0.98 ± 0.08	0.96 ± 0.07	**0.63 ± 0.05**
		L3b		0.85 ± 0.04	0.92 ± 0.04	0.89 ± 0.04
128	YES	L2b	9	1.03 ± 0.07	1.25 ± 0.08	1.09 ± 0.08
		L3b		0.91 ± 0.04	0.95 ± 0.04	0.90 ± 0.04

4. Discussion

The amount of measurement and computational data presented in the previous Section has been processed in order to determine parameters which allow a quantitative and concise comparison among the different models here considered. To this aim, for each considered set of results (i.e. a phantom configuration, a supply frequency and an investigation line) computational results (c) have been plotted versus the corresponding measurement points (m) and then fitted by linear interpolation ($c = a \cdot m$). As an example, Fig. 10 shows such plots, derived from computational and experimental data reported in Fig. 3, which correspond to the phantom radiated by the antenna #1 at 64 MHz. Similar plots can be obtained for data reported in Figs. 4 to 9 but they are omitted here for brevity.

The parameter a of the linear fit, determined by least-square minimization, provides a quantitative estimation of the overall goodness of the modeling result. A value of $a > 1$ indicates overestimation of computations, while $a < 1$ underestimation. The determination of fitting parameter a suffers from the uncertainty of measurement data. Thus, an expanded uncertainty $U(a)$ can be associated with this parameter, as explained in the Appendix. The values of a and $U(a)$, associated with quantities H_y/H_{ref}, H_z/H_{ref}, and E_x/H_{ref} are reported in Tables II to V, respectively for FIT(CST), FDTD(SEMCAD), BEM and FEM-BEM models. Values of parameter a greater than 1.3 or lower than 0.7 are highlighted in the tables.

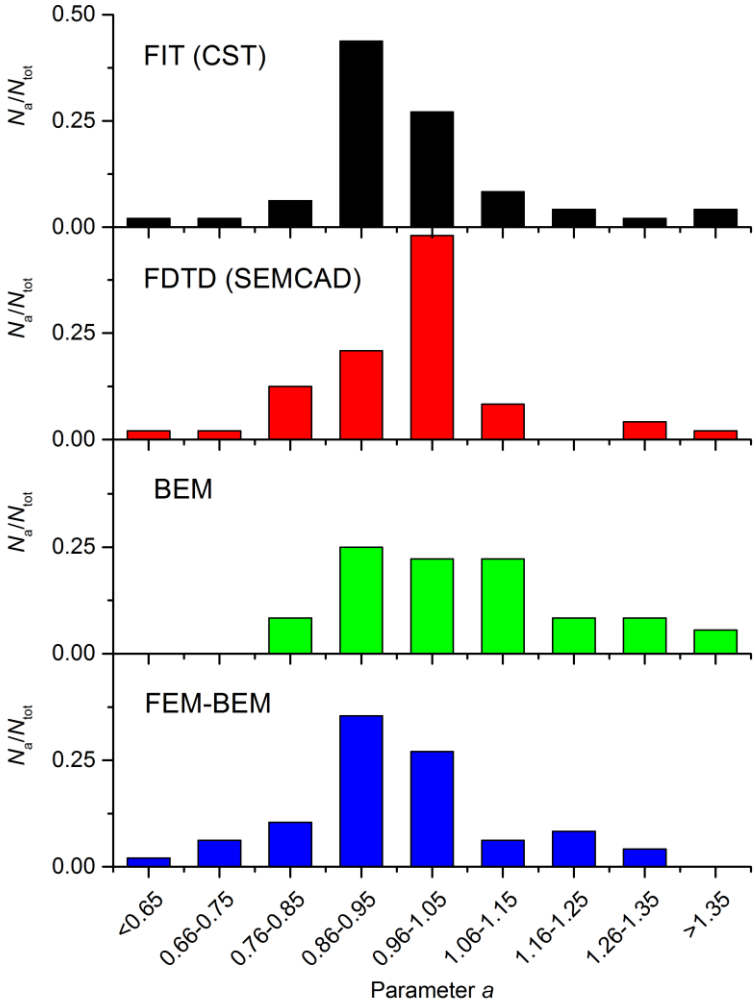

FIG 11. Frequency distribution of parameter a·for the considered computational methods. N_a is the number of values found in the corresponding range of parameter a and N_{tot} is the total number of results.

Considering the overall values of the parameter a as a statistical data, the frequency distributions are reported in Fig. 11, fixing the computational method and considering all simulated cases. The ratio N_a/N_{tot} is representative of the data frequency, being N_a the number of values found in the corresponding range of parameter a and N_{tot} the total number of results (see Tables II to V).

For FIT(CST) parameter a lies in the range 0.95 ÷ 1.05 on 13 of 48 cases investigated; it was < 0.95 on 26 occasions and was > 1.05 on 9 occasions. For FDTD(SEMCAD) corresponding figures are 23 (0.95 ÷ 1.05), 18 (< 0.95) and 7 (> 1.05), respectively, and for FEM-BEM they are 13 (0.95 ÷ 1.05), 26 (< 0.95) and 9 (> 1.05) , respectively. Finally for BEM there were 8, 12, and 16 cases of 36 for which a lies in the range 0.95 ÷ 1.05, was < 0.95, or was > 1.05, respectively. These global values provide a first estimate of the accuracy of model reconstruction. It should be noted that the corresponding values of expanded uncertainty $U(a)$ are almost randomly distributed and range from 0.04 to 0.12.

Going into a more specific analysis of each case considered, the results obtained with antenna #1 show in general good qualitative agreement and satisfactory quantitative agreement between experiments and computations (see Figs. 3, 4 and 5). The behavior of all spatial components of the magnetic **H** and electric **E** fields is quite well reconstructed by all methods, including the strong field gradient due to the vicinity of the source. However, the accuracy reduces as the frequency increases. At 64 MHz, the fitting parameter a ranges from 0.86 to 1.29 for FIT(CST), from 0.87 to 1.28 for FDTD(SEMCAD), from 0.86 to 1.34 for BEM and from 0.88 to 1.16 for FEM-BEM, considering the main field components (H_y, H_z and E_x). The corresponding uncertainty of the measured fields is about 15% (with a coverage factor k = 2). Higher local discrepancies (up to about 30% for the BEM results) are found along line L1a, in proximity of the phantom surface, for the y component of the magnetic field, which is not the prevailing one. The inaccuracy of BEM in close proximity of the surfaces is intrinsic to this method and is due to the presence of interface conditions.

Similar considerations hold at 128 MHz. The fitting parameter a ranges from 0.86 to 1.38 for FIT(CST), from 0.87 to 1.33 for FDTD(SEMCAD), from 0.87 to 1.40 for BEM and from 0.85 to 1.17 for FEM-BEM. The agreement between computations and measurements is generally satisfactory, apart in the proximity of the phantom boundaries (line L1a) for the lower magnetic field component (H_y) and at the extremities of line L2a for the electric field, where very low values are measured (less than 1 V/m), comparable to the "background" noise.

Modeling accuracy is slightly lower at 300 MHz for all methods. The fitting parameter a ranges from 0.75 to 1.39 for FIT(CST), from 0.75 to 1.38 for FDTD(SEMCAD), from 0.80 to 1.54 for BEM and from 0.83 to 1.29 for FEM-BEM.

As a general consideration, the model predictions when the phantom is radiated with antenna #1 are quite good. In this small loop the current is practically identical in all sections of the lead wire, so that the approximation of an ideal source with impressed current assumed in FEM-BEM and BEM models is in good agreement with the physical phenomena.

The set of results obtained with the setup configuration using antenna #2 shows overall discrepancies between computations and experiments that are comparable with those found for antenna #1. At 64 MHz, the fitting parameter a ranges from 0.86 to 1.22 for FIT(CST), from 0.81 to 1.10 for FDTD(SEMCAD), from 0.91 to 1.27 for BEM and from 0.71 to 1.09 for FEM-BEM. At 128 MHz, values of a range from 0.84 to 0.99 for FIT(CST), from 0.83 to 1.04 for FDTD(SEMCAD), from 0.9 to 1.33 for BEM and from 0.79 to 1.02 for FEM-BEM. Higher localized discrepancies are found with respect to antenna #1, with values up to 30% in the investigation regions for the results obtained in absence of the metallic object and for both the magnetic and electric field (see Figs. 6 and 7). With respect to the results with antenna #1, in this case an additional source of error arises due to the prediction of the current distribution between the main antenna lead and its shield, mainly affecting the near-field (Carobbi *et al* 2004). This effect is clearly evident in the spatial distribution of the fields along the vertical direction (line L3b). In particular, asymmetries in the diagram of the measured **H** field components can be attributed to a non-uniform distribution of the current within the lead and the shield and to the presence of the metallic box which houses the terminals and the capacitors. In contrast to the FIT and

FDTD approaches that intrinsically take into account the interactions between the elements of the antenna (apart from discretization inaccuracies), these effects are not considered in the approaches based on BEM and FEM-BEM, which assume the source as ideal. Higher quantitative and qualitative discrepancies are found using the BEM formulation, which seems to be less accurate in reproducing the phenomena arising within the liquid. Despite these additional effects, a total inaccuracy around 30% can be associated to simulations for this set of results.

The presence of the highly conductive metallic object within the phantom enhances differences using the different approaches (see Figs. 8 and 9). At the operating frequencies considered, this object acts as a shield for the EM field, as indicated by results from the plots of the **E** field along L2b line. The spatial distributions of the **H** and **E** fields in the TSL nearby the object are consequently altered, as shown in the plot along the vertical line L3. As a consequence, in the region very close to the metallic object, the electric field amplitude is reduced by 10% to 30% depending on the frequency and position. Overall discrepancies between simulations and experiments do not significantly vary from those obtained without the metallic object. However, a general tendency towards underestimation is found for all methods at 64 MHz. This effect results from the values of the fitting parameter *a*, which ranges from 0.65 to 0.95 for FIT(CST), from 0.63 to 1.02 for FDTD(SEMCAD), and from 0.63 to 0.98 for FEM-BEM at 64 MHz. At 128 MHz, the values range from 0.95 to 1.25 for FIT(CST), from 0.95 to 1.07 for FDTD(SEMCAD), and from 0.90 to 1.25 for FEM-BEM. Also for this set of simulations, a total inaccurracy around 30% can be associated to simulations.

The uncertainties found in the present study can be compared with others reported in the literature. For example Capstick *et al* 2008 simulated RF fields associated with several types of MR scanners and compared results with measurements of E- and H- fields. The results of simulations using FDTD and FIT approaches agreed within 6%, the uncertainty of the measurements was around 6-7%, and the uncertainty associated with predicted SAR values was about 50%, much of which arose from the generic nature of the RF coil models used in the simulations. In another study Kozlov *et al* 2010 reported agreement within 15% between results of simulations of the exposure of the human head to the RF field of a 7 T multi-channel coil carried out using HFSS (ANSYS, Canonsburg, PA) and FIT (CST Microwave Studio®).

5. Conclusions

In order to quantify the accuracy of EM simulations that predict the RF dosimetric exposure in typical MRI contexts, FDTD, FIT, BEM and FEM-BEM modeling approaches have been compared to measurements obtained from a customized phantom, surface antenna, and measurement system that provides controlled measurement conditions, enabling an accurate estimation of the uncertainty budget to be made. Attention has been focused on RF values of 64 MHz, 128 MHz, and 300 MHz, the operating frequencies of the most commonly used MRI systems with static magnetic fields of 1.5 T, 3 T and 7 T.

Results obtained show in general good qualitative agreement and satisfactory quantitative agreement between experiments and computations, although the differences increase as the frequency increases. Worst case discrepancies in modeling predictions of 30% were found for the E- and H-fields, associated with large field gradients obtained in the presence of metallic objects that simulated in a very simple way the presence of an implant.

Assessment of these differences in terms of a coefficient of linear interpolation, *a*, indicates that predictions of each numerical technique considered can overestimate ($a > 1$) or underestimate ($a < 1$) the corresponding measured data depending upon the field component (E_x, H_y, or H_z) and the direction considered (radial or vertical). For FIT parameter

a lies in the range 0.95 ÷ 1.05 on 13 of 48 cases investigated; for FDTD and FEM-BEM the corresponding figures are 23 and 13, respectively. Finally for BEM parameter *a* lies in the range 0.95 ÷ 1.05 on 8 cases of 36 investigated. Overall, FDTD performed slightly better than FIT and FEM-BEM. Predictions using BEM were less accurate.

An accurate evaluation of the different factors which affect the measurements in laboratory phantoms was also made to achieve a reliable uncertainty associated with electric and magnetic field measurements in the liquid phantom. A maximum extended uncertainty of 30% was associated with the experimental measurements.

The results are directly applicable to safety assessments of metallic implants and wires involving homogenous phantoms specified in some standards (eg ASTM F2182 Standard, 2011, ISO/TS 10974, 2012). Previous studies have shown that both FDTD and FIT are good at modelling complex heterogeneous geometries such anatomically realistic phantoms (Collins, 2009; Collins and Wang, 2011; Kozlov and Turner 2010). In these cases the uncertainty budget is more complex. In addition to the uncertainties in dielectric properties of tissues and the fact that relatively few phantoms are available to represent the human population, significant contributions to the uncertainty of predicted fields include the modelling of the RF transmit coil and the position and posture of the body relative to the coil.

Future activities will be focused on the comparison between simulations and experiments under more complex exposure conditions, including for example the use of birdcage to radiate the phantom and the local effects caused by the presence of realistic implants in patients undergoing MRI.

Appendix

Measurement model

In the present analysis, the measurand is the field component magnitude detected in the "target" point P_t (inside the TSL) at a temperature of (24 ± 3) °C. This quantity is not directly detectable owing to a number of influence quantities, in particular: *i*) the temperature oscillation occurring during the measurement stage (estimated to be limited within ± 3 °C), *ii*) the possible positioning errors of the field probes and *iii*) the probe inaccuracy. In the following, the discussion will deal with the magnetic field but the same description can be applied to the electric field.

In order to correct the systematic errors, as required by the JCGM, (2008) and to provide the best estimate H_{pt} of the magnetic field in the point P_t starting from the observed quantity H_{pg}, three correction coefficients are introduced in the model employed in the magnetic and electric field measurements:

$$H_{\mathrm{pt}} = H_{\mathrm{pg}} \cdot k_{\mathrm{cal}} \cdot M_{\Delta} \cdot \delta_{\mathrm{rep}}\left(\Delta T\right) \tag{A.1}$$

with

$$M_{\Delta} = \left(1 + \frac{\Delta}{\left(d_{\mathrm{s}} - d_{\mathrm{m}}\right)}\right)^{\alpha} \tag{A.2}$$

The coefficient M_{Δ} compensates for the positioning error between the actual measurement point P_g and the target one P_t; the coefficient $\delta_{rep}(\Delta T)$ takes into account the effect of the temperature oscillation on the electric properties of the TSL, and the coefficient k_{cal} is the calibration coefficient associated with the field probe.

In Eqn. A.2 Δ is the positioning error, d_s and d_m the *y*-coordinates, in the defined reference system, of the antenna plane and the point P_t, respectively. The maximum value of Δ is assumed to be equal to 2 mm, taking into account the accuracy of the positioning system. Moreover, preliminary experimental tests have shown that the averaging error introduced by the probes are negligible. The exponent α has been obtained by fitting the field decay along the *y*-axis and its value is ~1.5 in the considered measuring volume.

Simulations have estimated the effect of the temperature variation (estimated to be always less than ± 3 °C in the laboratory) on the electric and magnetic field within the liquid. The maximum differences in terms of field amplitudes found among the results at 21 °C and 27 °C, that is (24 ± 3) °C, are less than 2%. Consequently, assuming a rectangular distribution for temperature, the corresponding component to the uncertainty has been fixed equal to 0.01/√3.

The standard uncertainty of the measurand H_{pt} is obtained by applying the law of propagation of uncertainty (JCGM, 2008). In this first accuracy budget, all the quantities involved in A.1 are considered uncorrelated, thus the combined uncertainty $u_c(H_{pt})$ is given by:

$$u_c\left(H_{\mathrm{pt}}\right)=\sqrt{\sum_{\mathrm{i}=1}^{N}\left(\frac{\partial f}{\partial x_{\mathrm{i}}}\right)^2\cdot u^2\left(x_{\mathrm{i}}\right)} \tag{A.3}$$

where *f* is the function defined in Eqn. A.1 and $u(x_i)$ is the standard uncertainty associated with the influence quantity x_i. Since these are random variables, their rated values do not affect the measurement H_{Pg} but contribute to the combined uncertainty associated to H_{Pt}; they can take the following expression:

$$k_{\mathrm{cal}}=1\pm u\left(k_{\mathrm{cal}}\right);\ \delta_{\mathrm{rep}}\left(\Delta T\right)=1\pm u\left(\delta_{\mathrm{rep}}\right);\ \Delta=0\pm u\left(\Delta\right) \tag{A.4}$$

Since the difference between the magnitude of H_{pt} and H_{pg} is very low, the relative combined uncertainty $u_r(H_{pt})$, can be finally expressed as:

$$u_{\mathrm{r}}\left(H_{\mathrm{pt}}\right)=\frac{u\left(H_{pt}\right)}{H_{pt}}\cong\sqrt{\left(\frac{u\left(H_{\mathrm{pg}}\right)}{H_{\mathrm{pg}}}\right)^2+u_{\mathrm{r}}^2\left(k_{\mathrm{cal}}\right)+u_{\mathrm{r}}^2\left(\delta_{\mathrm{rep}}\left(T\right)\right)+\left[\alpha\cdot\frac{u\left(\Delta\right)}{d_{\mathrm{s}}-d_{\mathrm{m}}}\right]^2} \tag{A.5}$$

As shown in Eqn. A.5, four uncertainty contributions are considered. The component $u\left(H_{Pg}\right)$ takes into account the noise effect and the limited resolution of the acquisition system. It is a constant quantity and has the value of 0.001/√3 A/m and 1/√3 V/m for the magnetic and electric field probe respectively. The higher value associated with the electric field probe is due to the high noise level detected during such field measurement.

As an example of the uncertainty budget calculation, it is assumed the target point P_t {x = 0 m, y = 0.1 m, z = 0.184 m} where a value of H_{pg}=4 A/m has been measured. The uncertainty contributions are:

$u\left(H_{meas\_Pg}\right)=0.001/\sqrt{3}$ A/m	type B, rectangular PDF
$u_r\left(k_{\mathrm{cal}}\right)=0.03$	type B, gaussian PDF
$u_r\left(\delta_{\mathrm{rep}}\left(T\right)\right)\cong 0.01/\sqrt{3}$	type B, rectangular PDF
$u\left(\Delta\right)=0.002/\sqrt{3}$ m	type B, rectangular PDF

For each influence quantity, the standard uncertainty, the uncertainty type evaluation (as defined by JCGM (JCGM, 2008)) and the associated probability density function (PDF) are given. By applying Eqn. A.5, an expanded uncertainty $U(H_{pt})$ of 0.09 is obtained (with a coverage probability of 95%).

Finally, the relative standard uncertainty associated with the normalized quantity $H_{Nt} = H_{pt}/H_{ref}$ ($E_{Nt} = E_{pt}/H_{ref}$), is given by:

$$u_r(H_{Nt}) = \sqrt{u_r(H_{pt})^2 + u_r(H_{ref})^2};\ u_r(E_{Nt}) = \sqrt{u_r(E_{pt})^2 + u_r(H_{ref})^2} \tag{A.6}$$

where $u_r(H_{ref})$ is the relative standard uncertainty associated with the magnetic field in the reference point.

Fitting model for computational versus measurement results

For a given investigation line, computational results (c_i) obtained with a selected model (FIT, FDTD, etc.) are reported versus the N measurement data (m_i, with i=1,…N), obtaining the plots shown as an example in Fig. 10. These dispersed computed data (c_i) are fitted by a least-square minimization, using a linear interpolator with slope a:

$$c = a \cdot m \tag{A.7}$$

Coefficient a provides an estimate of the overall capability of the numerical method to reproduce experiments. If $a > 1$ or $a < 1$, the model either overestimates or underestimates, respectively, the experiments.

Since experimental data are affected by uncertainty, a related uncertainty can be associated with parameter a, following the rules for propagation of uncertainty. In particular, having applied the least square minimization algorithm, parameter a is given by:

$$a = \frac{\sum_{i=1}^{N} c_i m_i}{\sum_{i=1}^{N} m_i^2} \tag{A.8}$$

The uncertainty $u(a)$ associated to parameter a is defined as:

$$u^2(a) = \sum_{j=1}^{N} \left[\frac{\partial a}{\partial m_j} u(m_j) \right]^2 \tag{A.9}$$

having assumed that the measurement values are uncorrelated and $u(m_j)$ being the uncertainty associated to the measurement value m_j. In (A.9) the derivatives of a can be computed as:

$$\frac{\partial a}{\partial m_j} = \frac{c_i \sum_{i=1}^{N} m_i^2 - 2m_j \sum_{i=1}^{N} (c_i m_i)}{\left(\sum_{i=1}^{N} m_i^2 \right)^2} \tag{A.10}$$

Values of parameter a, with the corresponding expanded uncertainty $U(a)$ (coverage probability of 95%), are reported in Tables II to V.

Acknowledgments

This work was developed under the European Metrology Research Programme (EMRP)-HLT06 Joint Research Project (JRP) “Metrology for next-generation safety standards and equipment in MRI” (2012–2015). EMRP is jointly funded by the EMRP participating countries within EURAMET and the European Union.

Funding was also received from the Italian MIUR project “Metrology for therapeutic and diagnostic techniques based on electromagnetic radiation and ultrasound waves” (2014-2016).

Finally, we would like to thank Dr. Bernd Ittermann for his useful comments and suggestions.

References

Amjad A, Kamondetdacha R, Kildishev AV, Park S-M, and Nyenhuis JA 2005 Power deposition inside a phantom for testing of MRI heating, *IEEE Trans. Magn.* **41** (10) 4185-4187.

Andreuccetti D, Fossi R, and Petrucci C 2000 An internet resource for the calculation of the dielectric properties of body tissues. url: http://niremf.ifac.cnr.it/tissprop/.

ASTM F2182 Standard 2011 Test Method for Measurement of Radio Frequency Induced Heating On or Near Passive Implants During Magnetic Resonance Imaging.

Athey TW, Stuchly MA, Stuchly SS 1982 Measurement of radio frequency permittivity of biological tissues with an open-ended coaxial line: Part I, *IEEE Transactions on MTT*, 30, 82-86.

Bamba A, Joseph W, Vermeeren G, Tanghe E, Gaillot DP, Andersen JB, Nielsen JØ, Lienard M, Martens L Validation of experimental whole-body SAR assessment method in a complex indoor environment *Bioelectromagnetics* **34** (2) 122-132.

Bassen HI, and Mendoza GG 2009 In-vitro mapping of E-fields induced near pacemaker leads by simulated MR gradient fields, *BioMedical Engineering OnLine*, 8:39 doi:10.1186/1475-925X-8-39.

Bernardi P, Cavagnaro M, D'Atanasio P, Di Palma E, Pisa S, and Piuzzi E 2002 FDTD, multiple-region/FDTD, ray-tracing/FDTD: a comparison on their applicability for human exposure evaluation *International Journal of Numerical Modelling-electronic Networks Devices and Fields*, **15** (5-6), 579-593.

Botha CP, Preim B, Kaufman A, Takahashi S, and Ynnerman A 2012 From individual to population: Challenges in Medical Visualization, arXiv:1206.1148.

Bottauscio O, Chiampi M, and Zilberti L 2011 A Boundary Element Approach to relate surface fields with the specific absorption rate (SAR) induced in 3-D human phantoms Engineering Analysis with Boundary Elements 35 (4) 657-666.

Bottauscio O, Chiampi M, Zilberti L 2012 Boundary Element solution of electromagnetic and bioheat equations for the simulation of SAR and temperature increase in biological tissues, *IEEE Trans. Magn.* **48** (2), 691-694.

Bottauscio O, Chiampi M, and Zilberti L 2014 Massively parallelized Boundary Element simulation of voxel-based human models exposed to MRI fields, *IEEE Trans. Magn.* **50**(2), 7025504.

Bottauscio O, Chiampi M, Hand J, and Zilberti 2015 A GPU Computational Code for Eddy-Current Problems in Voxel-Based Anatomy IEEE Trans. Mag., 51 (3), 5100904.

Brebbia CA, and Walker S 1980 Boundary Element techniques in Engineering, Newnes-Butterworths, London.

Cabot E, Lloyd T, Christ A, Kainz W, and Douglas M 2013 Evaluation of the RF heating of a generic deep brain stimulator exposed in 1.5 T magnetic resonance scanners, *Bioelectromagnetics*, **34**(2) 104-113.

Capstick M, McRobbie D, Hand J, Christ A, Kűhn S, et al. 2008 An investigation into occupational exposure to electromagnetic fields for personnel working with and around medical magnetic resonance imaging equipment. Employment, Social Affairs and Equal Opportunities DG, European Commission. Available at: http://www.itis.ethz.ch/assets/Downloads/Papers-Reports/Reports/VT2007017FinalReportv04.pdf.

Carobbi C, and Millanta L 2004 Analysis of the common-mode rejection in the measurements and generation of magnetic fields using loop probes, *IEEE Trans. Instr. Meas.* **53** (2) 514-523.

Cimala C, Clemens M, Hansen V, Spathmann O, Streckert J, and Timm T 2013 High resolution numerical electromagnetic dosimetry simulations using a coupled two-step approach, *IEEE Trans. Magn.* **49** (5) 1633-1636.

Clemens M, Dickmann S, El Ouardi A, Hansen V, M. Schaarschmidt M, et al. 2012 Numerical dosimetry schemes for the simulation of human exposure to pulsed high-power electromagnetic-field sources *IEEE Trans. Magn.* **48** (2) 807-810.

Collins CM, and Smith MB 2003 Spatial resolution of numerical models of man and calculated Specific Absorption Rate using the FDTD Method: A study at 64 MHz in a Magnetic Resonance Imaging coil, *J. Magn. Reson. Imaging* **18** 383–388.

Collins CM 2009 Numerical Field Calculations Considering the Human Subject for Engineering and Safety Assurance in MRI *NMR Biomed.* **22** (9) 919–926.

Collins CM, and Wang Z 2011 Calculation of radiofrequency electromagnetic fields and their effects in MRI of human subjects *Magn. Reson. Med.* **65** 1470–1482.

D'Angelo J 1989 Hybrid Finite Element / Boundary Element analysis of electromagnetic fields, in Topics in Boundary Element Research, Volume 6: Electromagnetic Applications, Springer-Verlag, Berlin, 151-181.

de Raedt H, Michielsen K, Kole JS, and Figge MT 2003 Solving the Maxwell equations by the Chebyshev method: A one-step finite difference time-domain algorithm, *IEEE Trans. Antennas Propag.* **51** (11) 3155–3160.

Dimbylow PJ, and Gandhi OP 1991 Finite-difference time-domain calculations of SAR in a realistic heterogeneous model of the head for plane-wave exposure from 600 MHz to 3 GHz *Phys. Med. Biol.* **36**(8) 1075-89.

Directive 2013/35/EU of the European Parliament and of the Council amending Directive 2004/40/EC on the minimum health and safety requirements regarding the exposure of workers to the risks arising from physical agents (electromagnetic fields) (20th individual Directive within the meaning of Article 16(1) of Directive 89/391/EEC) and repealing Directive 2004/40/EC, 26 June 2013.

Elwassif MM, Datta A, Rahman A, Bikson M 2012 Temperature control at DBS electrodes using a heat sink: experimentally validated FEM model of DBS lead architecture *J. Neural Eng.* **9** 046009.

EN/IEC 60601-2-33, 2010, Medical electrical equipment – Part 2-33: Particular requirements for the safety of magnetic resonance equipment for medical diagnosis.

Gabriel C, Gabriel S, and Corthout E 1996a The dielectric properties of biological tissues: I. Literature survey *Phys. Med. Biol*. **41** 2231–2249.

Gabriel S, Lau RW, and Gabriel C 1996b The dielectric properties of biological tissues: II. Measurements in the frequency range 10 Hz to 20 GHz *Phys. Med. Biol.* **41** 2251–2269.

Gabriel S, Lau RW, and Gabriel C 1996c The dielectric properties of biological tissues: III. Parametric models for the dielectric spectrum of tissues *Phys. Med. Biol.* **41** 2271–2293.

Gajsek P, Walters TJ, Hurt WD, Ziriax JM, Nelson DA, and Mason PA 2002 Empirical validation of SAR values predicted by FDTD modeling *Bioelectromagnetics* **23** (1) 37–48.

Giordano D, Zilberti L, Borsero M, Forastiere R, and Wang W 2013 Experimental set-up for the validation of numerical methods in electromagnetic dosimetry *Proc. 19th Symposium IMEKO TC 4 Symposium and 17th IWADC Workshop, Advances in Instrumentation and Sensors Interoperability*, July 18-19, 2013, Barcelona, Spain.

Gorny KR, Presti MF, Goerss SJ , Hwang SC, Jang D-P, et al. 2013 Measurements of RF heating during 3.0-T MRI of a pig implanted with deep brain stimulator, *Magn. Reson. Imaging* **31** 783–788.

Hamada S 2011 GPU-accelerated indirect boundary element method for voxel model analyses with fast multipole method *Computer Physics Communications* 182 (5), 1162-1168)

Hasgall PA, Neufeld E, Gosselin MC, Klingenböck A, Kuster N 2013 IT'IS Database for thermal and electromagnetic parameters of biological tissues. Version 2.3, February 11th, 2013. www.itis.ethz.ch/database.

ICNIRP Guidelines for limiting exposure to time-varying electric, magnetic and electromagnetic fields (up to 300 GHz), 1998, *Health Physics*, **74** (4), 494-522.

ICNIRP Guidelines for limiting exposure to time-varying electric, magnetic and electromagnetic fields (up to 300 GHz), 2009, *Health Physics*, **97** (3), 257-258.

ICNIRP Statement Amendment to the ICNIRP "Statement on medical magnetic resonance (MR) procedures: protection of patients", 2009, *Health Physics*, **97** (3), 259-261.

ICNIRP Guidelines for limiting exposure to time-varying electric, magnetic and electromagnetic fields (1 Hz - 100 kHz), 2010, *Health Physics*, **99** (7), 818-836.

ICNIRP Guidelines for Limiting Exposure to Electric Fields Induced by Movement of the Human Body in a Static Magnetic Field and by Time-Varying Magnetic Fields below 1 Hz 2014 *Health Physics* **106** (3) 418-425.

Ilvonen S and Laakso I 2009 Computational estimation of magnetically induced electric fields in a rotating head *Phys. Med. Biol.* **54**, 341–51.

ISO/TS 10974, 2012, Assessment of the safety of magnetic resonance imaging for patients with an active implantable medical device.

JCGM 100:2008, Evaluation of measurement data — Guide to the expression of uncertainty in measurement (http://www.bipm.org/en/publications/guides/gum.html).

Kainz W, Woods T, Fiedler F, Hrdlicka G, Bobgan J, Schaefers G, Luechinger R, Szeverenyi N, Christ A and Kuster N 2009 Variation of whole body averaged phantom specific absorption rate (SAR), gel heating, and implant heating in seven different MR systems Proc. Asia-Pacific Symposium on Electromagnetic Compatibility and 19th International Zurich Symposium on Electromagnetic Compatibility (APEMC 2008), 19-23 May 2008, pp. 220 – 223.

Kozlov M, Turner R A 2010 Comparison of Ansoft HFSS and CST Microwave Studio Simulation Software for Multi-channel Coil Design and SAR Estimation at 7T MRI *PIERS Onlin*e **6** (4) 395-399.

Kangarlu A, Tang L, Ibrahim TS 2007 Electric field measurements and computational modeling at ultrahigh-field MRI *Magnetic Resonance Imaging* **25** 1222–1226.

Laakso I, and Hirata A 2012 Reducing the staircasing error in computational dosimetry of low-frequency electromagnetic fields *Phys. Med. Biol*. **57** N25–N34.

Liu Y, Liang Z, and Yang ZQ 2008 Computation of electromagnetic dosimetry for human body using parallel FDTD algorithm combined with interpolation technique *Progress In Electromagnetics Research*, *PIER* **82**, 95–107.

Li BK, Liu F, Weber E, Crozier S 2009 Hybrid numerical techniques for the modelling of radiofrequency coils in MRI *NMR Biomed.* **22**, 937–939.

Loader B, Gregory A, Bownds A, Johnson Y Non-toxic phantoms for SAR measurements (30 MHz to 6 GHz) 2010 2nd Annual Meeting of the Bioelectromagnetics Society 2010.

Mattei E, Calcagnini G, Censi F, Triventi M, and Bartolini P 2010 Numerical model for estimating RF-induced heating on a pacemaker implant during MRI: experimental validation, *IEEE Trans. Biomed. Eng.* **57** (8) 2045-2052.

Mohsin SA, Sheikh NM, Saeed U 2008 MRI-induced heating of deep brain stimulation leads *Phys. Med. Biol*. **53** 5745–5756.

Murbach M, Neufeld E, Capstick M, Kainz W, Brunner D, Samaras T, Pruessmann K, and Kuster N 2014 Thermal Tissue Damage Model Analyzed for Different Whole-Body SAR and Scan Durations for Standard MR Body Coils *Magn Reson Med*. **71** (1) 421-31.

Nagai T, Hirata A, and Fujiwara O 2009 Computational dosimetry on contact currents from charged human body *Proc. EMC'09*, Kyoto, Japan 465-468.

Nelson DA, Curran AR, Nyberg HA, Marttila EA, Mason PA, Ziriax JM 2013 High-resolution simulations of the thermophysiological effects of human exposure to 100 MHz RF energy Phys. Med. Biol. **58** 1947–1968.

Neufeld E, Kühn S, Szekely G, Kuster N 2009 Measurement, simulation and uncertainty assessment of implant heating during MRI *Phys. Med. Biol.* **54** 4151–4169.

Nguyen DT, Qin J, Sancer MI, McClary R 2002 Finite element-boundary integral methods in electromagnetics *Finite Elem. Anal. Des.* **38** (5), 391-400.

Nguyen UD, Brown JS, Chang IA, Krycia J, Mirotznik MS 2004 Numerical Evaluation of Heating of the Human Head Due to Magnetic Resonance Imaging *IEEE Trans. Biomed. Eng*. **51** (8), 1301-1309.

Oh S, Webb AG, Neuberger T, Park B-S, and Collins CM 2010 Experimental and numerical assessment of MRI-induced temperature change and SAR distributions in phantoms and in vivo, *Magn. Reson. Med.* **63** 218–223.

Oh S, Ryu Y, Carluccio G, Sica CT, Collins CM 2014 Measurement of SAR-Induced Temperature Increase in a Phantom and In Vivo with Comparison to Numerical Simulation *Magn. Reson. Med* **71**, 1923–1931.

Pisa S, Cavagnaro M, and Piuzzi E 2005 Numerical-experimental validation of a GM-FDTD code for the study of cellular phones, *Microw. Opt. Techn. Let.* **47** (4) 396-400.

Powell J, Papadaki A, Hand J, Hart A, and McRobbie D 2012 Numerical simulation of SAR induced around Co-Cr-Mo hip prostheses in situ exposed to RF Fields associated with 1.5 and 3 T MRI body coils, *Magn. Reson. Med.* **68** 960–968.

Ruoff J, Wurslin C, Graf H, and Schick F 2012 Resolution Adapted Finite Element Modeling of Radio Frequency Interactions on Conductive Resonant Structures in MRI *Magn. Res. Med*. 67 1444–1452

Samaras T, Regli P, and Kuster N 2000 Electromagnetic and heat transfer computations for non-ionizing radiation dosimetry *Phys. Med. Biol*. **45** (8) 2233-2246.

Stuchly MA, Athey TW, Samaras CM, Taylor GE 1982 Measurement of radio frequency permittivity of biological tissues with an open-ended coaxial Line: Part II - Experimental results, *IEEE Transactions on MTT*, 30, 87–92.

van den Berg CAT , Bartels LW, van den Bergen B, Kroeze H, de Leeuw AAC, et al. 2006 The use of MR B_1^+ imaging for validation of FDTD electromagnetic simulations of human anatomies *Phys. Med. Biol*. **51** (19), 4735-4746.

van Lier ALHMW, Kotte ANTJ, Raaymakers BW, Lagendijk JJW, and van den Berg CAT 2012 Radiofrequency heating induced by 7T head MRI: thermal assessment using discrete vasculature or Pennes' Bioheat Equation *J. Magn. Reson. Imaging* **35** 795–803.

Wang Z, Lin JC, P, Mao W, Liu W, Smith MB, Collins CM 2007 SAR and Temperature: Simulations and Comparison to Regulatory Limits for MRI *J. Magn. Reson. Imaging* **26** 437–441.

Voigt T, Homann H, Katscher U, and Doessel O 2012 Patient-individual local SAR determination: in vivo measurements and numerical validation *Magn. Reson. Medicine*, **68** (4), 1117-1126.

Wolf S, Diehl D, Gebhardt M, Mallow J, Speck O 2013 SAR Simulations for High-Field MRI: How Much Detail, Effort, and Accuracy Is Needed? *Mag. Reson. Med*. **69** 1157–1168.

Weiland T 1977 A Discretization Method for the Solution of Maxwell's Equations for Six-Component Fields *Electronics and Communications AEUE* **31** (3) 116–120.

Wilkoff BL, Albert T, Lazebnik M, Park S_M, Edmonson J, et al. 2013 Safe magnetic resonance imaging scanning of patients with cardiac rhythm devices: A role for computer modeling, *Heart Rhythm* **10** (12) 1815-1821.

Yee K 1966 Numerical solution of initial boundary value problems involving Maxwell's equations in isotropic media *IEEE Trans. Antennas Propag*. 14 (3) 302–307.

Zelinski AC, Goyal VK, Adalsteinsson E, Wald LL 2008 Fast, accurate calculation of maximum local N-gram Specific Absorption Rate *Proc. Intl. Soc. Mag. Reson. Med*. **16** 1188.

Zhang X, Schmitter S, Van de Moortele P-F, Liu J, and He B 2013 From complex mapping to local SAR estimation for human brain MR imaging using multi-channel transceiver coil at 7T, *IEEE Transactions on Medical Imaging* **32** (6) 1058-1067.